

ABSTRACT**PHOTOINJECTOR GENERATION OF HIGH-CHARGE
MAGNETIZED BEAMS FOR ELECTRON-COOLING APPLICATIONS**

Aaron Thomas Fetterman, M.S.
Department of Physics
Northern Illinois University, 2020
Dr. Philippe Piot, Director

The recently announced Electron-Ion Collider (EIC), to be built at Brookhaven National Laboratory, will collide high-energy ion-beams and electron beams to pursue nuclear physics research on quark-gluon plasma's. The facility performances (luminosity) would be improved if the ion-beam emittance degradation is mitigated via a phase-space-cooling technique. One potential cooling method uses a bright electron beam to cool the ion beams. The cooling rate for this electron-cooling method depends on the transverse emittance of the cooling electron beam and could benefit from using a beam with significant canonical angular momentum dubbed as a magnetized beam.

This research focuses on simulation and experimental generation and characterization of high charge magnetized electron beams with parameters comparable to those required for electron cooling at an electron-ion collider. The experiment uses the 50-MeV photoinjector available at the Fermilab Accelerator Science and Technology (FAST) Facility. The measurements are bench marked against simulations.

NORTHERN ILLINOIS UNIVERSITY
DE KALB, ILLINOIS

DECEMBER 2020

**PHOTOINJECTOR GENERATION OF HIGH-CHARGE
MAGNETIZED BEAMS FOR ELECTRON-COOLING APPLICATIONS**

BY

AARON THOMAS FETTERMAN
© 2020 Aaron Thomas Fetterman

A THESIS SUBMITTED TO THE GRADUATE SCHOOL
IN PARTIAL FULFILLMENT OF THE REQUIREMENTS
FOR THE DEGREE
MASTERS OF SCIENCE

DEPARTMENT OF PHYSICS

Thesis Director:
Dr. Philippe Piot

ACKNOWLEDGEMENTS

Special thanks to my advisor Dr. Philippe Piot for the wonderful research experience and mentor-ship. I would also like to thank my thesis defense committee members, Dr. Michael Syphers and Dr. Yasuo Ito, for their patience, time and effort in assisting in editing this thesis.

I also appreciate all of the professors who I have had the privilege of interacting with at Northern Illinois University, especially the ones who pushed me. And also, to all my fellow graduate students who I have been able to work along side on the blackboard and learn from, be inspired by, laugh with, and grow with. I hope to be able to work with all of you in the future.

And to the unsung hero's of the physics department, Jane, Carlos and Greg, without whom I would not have been able to get this far towards graduation.

Lastly, however most importantly, this work would not have been possible if it were not for my lovely wife Courtney and my ever enthusiastic children Grace and Emma. They deserve this degree just as much as I with all the sacrifices they have made in supporting their Husband or father. Thank you for the hugs and kisses before I go to work and when I come home. I have been blessed and am so grateful to be a member of such a loving family.

DEDICATION

This work is dedicated to my family, whom I love and cherish very much.

TABLE OF CONTENTS

	Page
List of Tables	vi
List of Figures.	vii
Chapter	
1 Introduction.	1
1.1 Motivation: The Electron-Ion-Collider	1
1.2 Beam Emittance	3
1.3 Electron Cooling	5
1.4 Performing Experiments at FAST.	7
2 Characterization and Generation of Magnetized Electron Beams.	9
2.1 Magnetized Electron Beams	9
2.2 Generation of Magnetized Electron Beams.	12
2.2.1 Partition of Eigen-Emittances	14
2.2.2 Emittance Measurements of Magnetized Beams.	16
3 Simulations of Magnetized Beams	18
3.1 Simulation Software.	18
3.2 Input Beam Distributions	20
3.3 Measuring the eigen-emittances	22
3.3.1 Mapping technique using round-to-flat beam transformer	22
3.3.2 Measurement using the Scanning Slit Technique	24
3.4 Observation of Peripheral Halo Formation.	28

Chapter	Page
4 Experiments at the FAST Facility	30
4.1 Experimental Setup	30
4.2 Measurement Methods and Analysis	31
4.2.1 Magnetization at the Cathode	32
4.2.2 Round to Flat Beam Transformation Method	33
4.2.3 Magnetization from Beam Slit Measurements	36
4.3 Experimental Measurements	37
4.3.1 RFBT Eigen-Emittance Mapping Experiment	38
4.3.2 Magnetization from Slit Measurements	41
4.4 Comparison of Theory, Simulations and Experiments	46
5 Conclusion	51
5.1 Summary	51
5.2 Future Work	52
References	54

LIST OF TABLES

Table		Page
1.1	Comparison for the electron-cooling beam requirements for the JLEIC parameters and corresponding value (inferred from simulations) achievable at FAST. All values are RMS quantities and the emittances are normalized. . . .	8
4.1	Summary of beam parameters and magnetization measurements of the RTFB emittance measurement data compared to the cathode magnetization measurement data. ε_u is the uncorrelated emittance and \mathcal{L} (exact) uses Eq. 2.9 with the eigen emittances and solves for ε_u and \mathcal{L}	39

LIST OF FIGURES

Figure		Page
1.1	Example of phase-space density in (x, x') space.	5
2.1	Demonstration of the transverse space of a magnetized electron beam with each vector pointing in the particles momentum direction. Used from Jefferson laboratory at https://wiki.jlab.org/ciswiki/index.php/File:MagBeam.JPG . 10	
2.2	Example set up for a photo-cathode electron beam source. The red dotted line represents the axial magnetic field (B_z). After the beam leaves the axial magnetic field the Canonical Angular Momentum changes to angular momentum of the beam. Figure used from Dr. Philippe Piot.	12
2.3	An example of the partition of eigen emittances from Eq. 2.9 with the accompanying high magnetization assumptions. An uncorrelated emittance of $10 \mu m$ has been used for demonstration.	16
3.1	The whole linear portion of the accelerator beam line at FAST. There is also an exit for electrons to be shot into the Integrable Optics Test Accelerator (IOTA) just downstream from the blue dipole labeled D604	19
3.2	Evolution of beam size in the FAST accelerator. Simulated using Imapact-Z and ELEGANT. This offered verification between the two simulation software's and was used later for other comparison studies as well.	20
3.3	Virtual cathode image (left) and corresponding Monte-Calro generated macro-particle distribution (right).	21
3.4	Evolution of eigen, conventional and 4D emittances along a RFBT section for the two possible solutions. The color bars represent the positions and lengths of the skew quadrupoles that form the RFBT.	24

Figure	Page
3.5 Transverse distribution simulated with Elegant, Impact-T and Impact-Z. Simulations of a magnetized beam at observation points X111 and X113 (positioned at 10.54 and 11.35 meters away from the photo-cathode injector).	25
3.6 Sample of simulating the slits emittance experiment for the LDRD experiment down stream of the cryo-module at FAST. Top left is a x-y space density plot with top right being a simulation of 11 evenly spaced positioned slits and letting the macro particles be transported though a drift space of 2 meters. The bottom left shows those same particles but just turned so that the beams effective beam size projection is decreased. Bottom right is the beam sizes for each of the x and y directions.. . . .	27
3.7 Radial distribution of the charge in a linear plot (top) and logarithmic (bottom) plots.	29
4.1 The Fermilab Accelerator Science and Technology (FSAT) facilities electron beam injector. Each of the purple labels of X... includes a Transverse Profile Monitor (TPM) allowing for pictures of the transverse beam shape to be taken at these locations. The Green rectangles represent quadrupoles that are used for focusing the electron beam. The three orange rectangles, labeled RFBT, are skew quadrupoles (quadrupoles axially turned 45 degrees). These allow for a magnetized electron beam to be transformed into a flat beam. . .	31
4.2 Contour plot of the magnetic field on the cathode as a function of the main and bucking solenoid currents.	33
4.3 Example of virtual cathode Image analysis for measurement of the beam sigma size. This is used as a reference for measurements of the electron beam dynamic magnetization's.	34
4.4 RFBT data from Run 1. Flat beam at X118 (top), Horizontal slits measuring the larger emittance (middle) and vertical slits measuring the smaller emittance (bottom).	40
4.5 Schematic of slit experiment at FAST.	41
4.6 Example of image analysis process. Taking the raw data (top row) and subtract the background noise image still resulted in a noisy projection (middle row). Next apply a median filter algorithm and a zeroing threshold for anything less than three percent of the maximum (bottom row).	43

Figure		Page
4.7	Example of data for the BPM data in the x and y directions and the intensities at the relative positions calculated from similar triangles from the BPM data. there are three data lines for each of the iterations of data collection.	45
4.8	Eigen emittance plus experimental data plotted against the calculated magnetization for the 3.2 nC case	47
4.9	Eigen emittance plus experimental data plotted against the calculated magnetization for the 1.6 nC case	48
4.10	Eigen emittance minus experimental data plotted against the calculated magnetization for the 3.2 nC case	49
4.11	Eigen emittance minus experimental data plotted against the calculated magnetization for the 1.6 nC case	50

CHAPTER 1

INTRODUCTION

1.1 Motivation: The Electron-Ion-Collider

The recently announced Electron-Ion Collider, (EIC), to be built at Brookhaven National Laboratory, will be built in the effort to better understand the structure inside the nucleus [1]. The EIC will collide electron beams against ion beams to probe the nuclei of a high energy ion beam in greater detail than previously achievable, resulting in measurements of the quark gluon-plasma in high energy ions and protons.

One important parameter when designing a colliding accelerator is the luminosity defined as the interaction rate of two beams in a given cross-section,

$$\mathbf{L} = f \frac{N_I N_e}{A} \tag{1.1}$$

where f is the frequency of bunch collisions per second, N_I and N_e are the number of ions (or protons) and electrons in the colliding bunches respectively and A is the cross-sectional area of the beam colliding beams [2]. Because each of these variables of the beam can be controlled in the design luminosity, \mathbf{L} , represents a single product of the variables that are controllable when considering designs of a collider. Maximizing the luminosity makes it more likely to measure rare collision events and can make necessary data collection orders of magnitude shorter in time. Thus for time and cost-effectiveness, this makes \mathbf{L} an important attribute to maximize when optimizing design plans. The necessary base luminosity for the EIC design parameters is on the order of $10^{34} \text{ cm}^{-2}\text{s}^{-1}$.

For the colliding hadron beam, it has been concluded that for the required \mathbf{L} to be achieved there will need to be a method to make the cross-sectional area smaller. One proposed method to achieve this is called electron cooling [3]. Electron cooling is a method where an electron beam and a hadron beam co-propagate together and are allowed to interact. Separate from the colliding electron beam, the cooling electron beam interact with the ion beam traveling in the same direction for a small section of the accelerator. This allows for the ion beam to be focused to a smaller cross sectional area before collision with the colliding electron beam. The basic mechanics of electron cooling will be discussed later in this chapter. The present research however focuses on the electron beam characteristics needed for electron cooling. Specifically, this research investigates the generation of the required electron beam parameters necessary for electron cooling.

This first chapter introduces some of the basics to describe electron beam dynamics. Concepts like emittance and some necessary details on Electron Cooling are introduced. Chapter 2 gives an introduction of the theory behind generating a magnetized beam and some ways to measure it. Chapter 3 describes the various tools used for numerical simulations. The next chapter, chapter 4 explains the experimental data collected in support for this research as well as results from the analysis. Finally, chapter 5 concludes with suggestions of future research directions.

The work presented in the thesis was performed in support of the electron cooling scheme proposed for the Thomas Jefferson Laboratory Electron-Ion Collider (JLEIC). Ultimately, the Brookhaven National Laboratory proposal of the electron-ion collider (EIC) was selected for construction but our study is still relevant to the EIC though conventional electron cooling is not including in the baseline design.

1.2 Beam Emittance

The concept of emittance, is central to quantifying the quality of a beam. Emittance describes the phase-space area occupied by a collection of particles composing the beam. Phase space is a concept that represents all possible positions and momentum's of a system in a two dimensional space. A single phase space is typically measured in the X or Y directions. It can have units of length (μm) or length-radians (mm-mrad). In this research we will use units of length (μm) which is customary for electron beam measurements.

Starting with canonical coordinates of a free particle there are three position coordinates, x, y, z , and three momentum coordinates, P_x, P_y, P_z . One convention is to refer to the direction of acceleration as the z direction making the x and y directions the transverse coordinates. Further more, because P_z will be so much bigger than P_x or P_y , we also define $x' = P_x/P_z$ and $y' = P_y/P_z$. This also means that the z momentum spread is now defined as $\delta = \Delta P_z/P_z$. With a new set of canonical conjugated coordinates $(x, x', y, y', z, \delta)$ a definition for the emittance can now be made.

Because the considered system has large numbers of particles, averaging the position and momentum spaces over the whole beam distribution can help calculate for emittance. The distribution of many particles over a phase-space will be referred to as $f(x, x')$. The following second order moments will be used in the calculation of emittance

$$\langle x^m x'^m \rangle = \int_{-\infty}^{\infty} x^m x'^m f(x, x') dx dx', \quad (1.2)$$

we also assume in this case that the beam is centered on the x and y axis so that the mean of the position is zero ($\langle x \rangle = \langle y \rangle = 0$). The transverse emittance is defined as

$$\varepsilon_x = \sqrt{\langle x^2 \rangle \langle x'^2 \rangle - \langle x x' \rangle^2} \quad (1.3)$$

where $\langle x^2 \rangle$ is the average squared position of the electron bunch in the x direction, also known as sigma size, $\langle x'^2 \rangle$ is the average divergence of each electrons position in the electron beam, and $\langle xx' \rangle$ is the correlation between the two. Unless stated otherwise the emittances reported in this thesis are normalized defined as

$$\varepsilon_{n,x} = (\beta\gamma)\varepsilon_x \quad (1.4)$$

where β is the reduced average speed of the bunch and γ is the relativistic Lorentz factor

$$\gamma = \frac{1}{\sqrt{1 - \beta^2}}. \quad (1.5)$$

In our case because we are routinely working with relativistic speeds ($E \approx 30$ MeV and $\beta \approx 0.9998$) we will approximate β to be 1. In summary the lower the spot size or the divergence from that spot size the lower the emittance. As a visual example of what emittance is a plot is given of an example phase space in x and x' in Fig. 1.1. Emittance can visually be explained as the amount of area this example phase-space occupies with units of length.

An important concept that comes with the idea of emittance is Liouville's theorem. Liouville's theorem states when working with Hamiltonian equations of motion for many objects, the phase space density is conserved [4]. Because the beam motion in the absence of space charge can be approximately described by a Hamiltonian system, the emittance in the x direction is conserved as a consequence of Liouville's theorem. While this is a good approximation it is also necessary to investigate through simulations and experiment the impacts of space-charge.

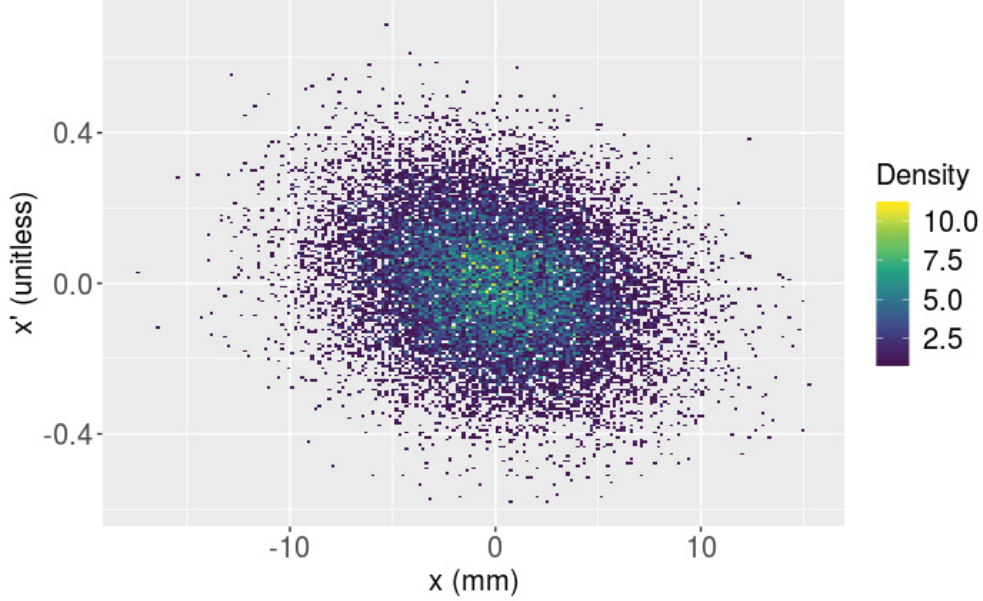


Figure 1.1: Example of phase-space density in (x, x') space.

There will be different types of emittances used throughout this thesis. They include eigen emittances, correlated and uncorrelated emittances, drift and cyclotron emittances, and effective and thermal emittances. Each one will be explained in chapter 2.

1.3 Electron Cooling

Electron Cooling, first proposed by G. I. Budker in 1966 [3], is a method to decrease the phase space of an ion beam. It is done by co-propagating a electron beam of the same speed but smaller emittance than the proton beam for a portion of a circular accelerator storage ring. This allows for the coulomb forces to interact creating scattering of the electrons and the proton/Ion beam. This creates an effective frictional force that mixes the two beams emittance and thus reduces the emittance of the proton beam. The lower emittance electron beam will also be replenished thus allowing for the lower emittance to stay low and not be increased by the mixing of the Coulomb scattering. If repeated many times, such as the

repetition in a colliding ring, this will bring the proton or ion beam into thermal equilibrium with the lower emittance electron beam. The method of electron cooling has produced much theoretical research [5] and experimental results [6].

One aspect that can make electron cooling more efficient is if the interaction time for the hadrons and the electrons have a longer or stronger interaction. This will decrease the needed interaction time to come to equilibrium for the two systems. This can be done by using a cooling solenoid section for the interaction length. The idea is that if there is any transverse momentum, the Lorentz force will cause the electron to circle in Larmor helixes with radius

$$r_L = \frac{v_{e\perp}}{eB_z} \quad (1.6)$$

where $v_{e\perp}$ is the electron beams transverse velocity, e is the fundamental charge and B_z is the cooling solenoid magnetic field [7]. The end result an increase in cooling interaction duration that can increase the cooling rate by a factor of

$$\tau = \frac{v_{e\perp}}{v - v_{e\parallel}} \quad (1.7)$$

where v is the longitudinal speed of the hadron or ion beam and $v_{e\parallel}$ is the longitudinal speed of the electron beam. Because the denominator of this factor can be made much smaller than the numerator. Thus making this introduction of the cooling solenoid an efficient alternative.

Another step further that can make electron cooling even more efficient is by making the transverse emittance of the electron beam even smaller. This can be done by making the cooling electron beam magnetized and matching the beam dynamics to introduce an even smaller angular emittance upon entry to the cooling solenoid [8]. The design is that if a magnetized electron beam can be matched with a cooling Solenoid section, the ε_- emittance would be mapped in the transverse . This makes it so that the eigen emittances separate,

the eigen minus emittance is mapped to the divergence of the emittance portion and the eigen plus emittance is mapped to the position portion of emittance [9]. This mapping is accomplished by matching the magnetization's of the cooling electron beam gun and a cooling solenoid [10] by way of

$$B_{cath}\sigma_{cath}^2 = B_{sol}\sigma_{sol}^2 \quad (1.8)$$

where B_{cath} is the axial magnetic field at the cathode, B_{sol} is the axial magnetic field in the cooling solenoid, σ_{cath} is the spot size at the cathode and σ_{sol} is the spot size at the entrance of the cooling solenoid. Later in section 2.2 it will be clear that this is a matching of the magnetization of the two positions

In summary our goal is to show that the required emittance specifications for electron cooling are achievable within reason for the promise of electron cooling.

1.4 Performing Experiments at FAST

To experimentally verify that high-charge magnetized electron beams could deliver the required emittances for electron cooling, a facility of similar electron beam qualities had to be used.

FAST was selected to explore the generation of magnetized electron beam due to its ability to produce electron bunched with properties comparable to those required for the proposed JLEIC electron cooler. The capability to attain 3.2 nC per bunch was especially critical. Table 1.1 describes the similarities of FAST to the requirements for the JLEIC, for which this research for initially. The parameters that do not match are the slice fractional momentum spread and peak current. However, because this would not affect the beam

Table 1.1: Comparison for the electron-cooling beam requirements for the JLEIC parameters and corresponding value (inferred from simulations) achievable at FAST. All values are RMS quantities and the emittances are normalized.

Parameter	Unit	JLEIC	FAST
Beam Energy	MeV	[20,55]	45
Beam Charge	nC	1.6/3.2	>3.2
cath. spot size	mm	1.1	1
B field on cath.	T	0.05	< 0.09
cyclotron emitt.	μm	≤ 19	< 5
drift emitt.	μm	36	37
$\delta p/p$ (uncor.)	-	$3 \cdot 10^{-4}$	< $4 \cdot 10^{-4}$
$\delta p/p$ (pk-to-pk.)	-	< $6 \cdot 10^{-4}$	$\mathcal{O}(10^{-2})$
bunch length σ_z	cm	2	0.2

magnetization, FAST facility was deemed to be a good testbed for the experiment reported in this Thesis.

The stated goals of $36 \mu\text{m}$ of drift emittance and $\leq 19 \mu\text{m}$ are the goals that we are looking to achieve. The drift and cyclotron emittances will be later defined as the eigen emittances also used in [10] which will be introduced in chapter 2.

CHAPTER 2

CHARACTERIZATION AND GENERATION OF MAGNETIZED ELECTRON BEAMS

2.1 Magnetized Electron Beams

A magnetized electron beam is one that has significant canonical angular momentum (CAM). Having also been termed as an angular-momentum-dominated beam [11], CAM beams have a conserved angular momentum with the presence of an axial magnetic field. Generation of a magnetized electron beam will be discussed in section 2.2. A pictorial example of this can be seen in Fig. 2.1.

One important parameter is to set a measurement for the amount of CAM in an electron beam distribution. The variable \mathcal{L} , which we will call magnetization, will be used to describe the amount of CAM for a given beam distribution. First, the notation of the beam distribution will be established to set the stage for understanding the amount of magnetization in a given particle beam.

A common way to describe a beam distribution is by referring to the transverse space second order beam moments. In this representation we assume similarly as in section 1.2



Figure 2.1: Demonstration of the transverse space of a magnetized electron beam with each vector pointing in the particles momentum direction. Used from Jefferson laboratory at <https://wiki.jlab.org/ciswiki/index.php/File:MagBeam.JPEG>.

that $\langle x \rangle = \langle y \rangle = 0$. This second order moment representation can be organized by the 4x4 matrix show below.

$$\Sigma = \begin{pmatrix} \langle x^2 \rangle & \langle xx' \rangle & \langle xy \rangle & \langle xy' \rangle \\ \langle x'x \rangle & \langle x'^2 \rangle & \langle x'y \rangle & \langle x'y' \rangle \\ \langle yx \rangle & \langle yx' \rangle & \langle y^2 \rangle & \langle yy' \rangle \\ \langle y'x \rangle & \langle y'x' \rangle & \langle y'y \rangle & \langle y'^2 \rangle \end{pmatrix} \quad (2.1)$$

where the x and y variables are referring to the x and y directions and the x' and y' variables are referring to the x and y divergences as explained in section 1.2. The averaging $\langle \rangle$ is done over all particles in the beam distribution. For a given particle with coordinates x, x', y, y' you can calculate the individual components for the matrix and then average the components

over the beam distribution. Seeing this second order matrix representation it is easy to show that the 2x2 (x, x') sub-block of the matrix

$$\begin{pmatrix} \langle x^2 \rangle & \langle xx' \rangle \\ \langle x'x \rangle & \langle x'^2 \rangle \end{pmatrix} \quad (2.2)$$

can be used to calculate the emittance in the x direction by way of the determinate. The same thing can be said of the 2x2 (y, y') sub-block of the Σ matrix.

Using the above as the notation of describing a distribution, a definition of magnetization, or CAM, can be made. Knowing that an angular momentum is present when there is a non-zero average for $\langle xy' \rangle$ and $\langle yx' \rangle$ components of the distribution above, the off-axis components in the upper right 2x2 matrix are used to calculate the amount of CAM in a beam distribution

$$2\mathcal{L} = \langle xy' \rangle - \langle yx' \rangle \quad (2.3)$$

Because angular momentum manifests as a correlation between x position and y momentum for instance, it makes sense to be using the off-axis 2×2 matrix values to calculate this constant value. For the case of a non-magnetized beam with no CAM, and thus no correlation between the x position and the y momentum, the off axis contributions used in Eq. 2.3 will go to zero. This makes it so that the emittances can be summaries with the x and y directions.

While a electron beam has emittances that are primarily focused on having emittances in the x and the y direction there is another way of keeping track of the emittances as well: eigen emittances. This is further discussed in the next section 2.2.

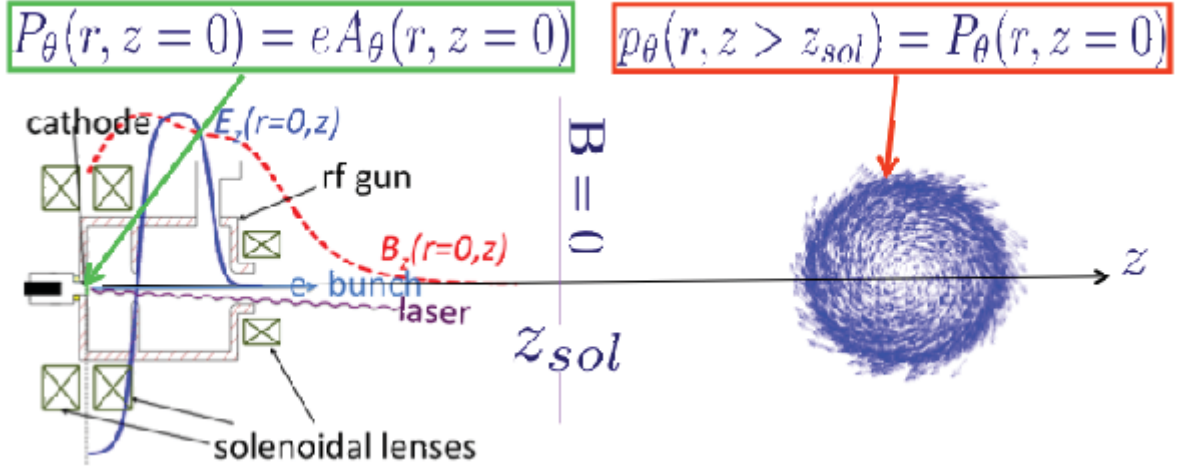


Figure 2.2: Example set up for a photo-cathode electron beam source. The red dotted line represents the axial magnetic field (B_z). After the beam leaves the axial magnetic field the Canonical Angular Momentum changes to angular momentum of the beam. Figure used from Dr. Philippe Piot.

2.2 Generation of Magnetized Electron Beams

Traditionally, strong solenoid magnets are used at the electron gun to focus low energy beams. Any number from one to three focusing solenoids can be used near the electron gun to control the magnetic fields at and just after the cathode. At the FAST facility there are two solenoids, the bucking and the main solenoids, positioned behind the photo-cathode and downstream of the cathode respectfully. Each solenoid is capable of reaching magnetic fields of 0.1 T. An example diagram of a solenoid set up on a photo cathode is depicted in Fig. 2.2.

When a traditional electron beam is desired, the solenoid magnets will be set so that the magnetic field is zero at the cathode. As soon as the electron bunch is emitted there are a couple of competing processes that control the beam dynamics in the source. One is space charge effects arising from the repulsive coulomb force of the electron bunch on its self. This

creates transverse velocities of the beam going away from the center of the beam, making the transverse size larger. Secondly, the electric field of the photo-cathode gun, which is designed to minimize the space charge effect, accelerates the bunch with large electric fields to higher energies. The space-charge force strength scales inversely with relativistic Lorentz factor squared ($1/\gamma^2$) [2]. Accelerating the bunch as quickly as possible minimizes the strength of space charge effects on the bunch. If the space charge effects interact too long on the beam in low energies the beam emittance will significantly degrade.

When a magnetized beam is desired, the conventional way to generate it is by setting the photo-cathode focusing solenoids so the axial magnetic field on the cathode is non-zero. Because the magnetic field is non-zero, there is a magnetic vector potential field, A_θ , only in the θ direction as in Ref. [12]

$$\mathbf{A}_\theta = \frac{B_0}{2} f(z) r \quad (2.4)$$

where B_0 is the axial magnetic field strength at the cathode, $f(z)$ is a function to describe the magnetic field for the injector solenoid set up and in this case $f(z = 0) = 1$, and r is related to the radius of the beam spot size. Also see Fig. 2.2 for a visual representation of the CAM. This creates a CAM dominated beam.

This CAM in the electron beam is transferred to mechanical angular momentum as the beam leaves the axial magnetic field created from the solenoids at the cathode. The kinetic angular momentum is most especially seen with tools such as the emittance slit measurements. In the example of the slit a small portion of an electron beam is allowed to propagate through the accelerator structure. In the case of a CAM beam the slit will allow particles to travel through that have angular momentum and will make the slit appear to 'turn' or 'shear'. This characteristic can be measured and shown to be related to the magnetization of the beam.

Put simply, there is a CAM that is introduced when the cathode is immersed in a axial magnetic field. The amount of CAM that is introduced can be related to the axial magnetic field and the beam size at the cathode by the equation

$$\gamma\mathcal{L} = \frac{eB_c}{2mc}\sigma_c^2 \quad (2.5)$$

where $\gamma\mathcal{L}$ is referred to as the normalized magnetization. Magnetization in this work will refer to normalized magnetization, unless otherwise stated. Equation 2.5 can be rewritten in engineering units as

$$\mathcal{L}[\mu m] \simeq 294B_c[T](\sigma_c[mm])^2 \quad (2.6)$$

2.2.1 Partition of Eigen-Emittances

If there is a magnetization in a beam, there will be an increase in the projected x and y emittances. This is because of the increased divergence from the particles position in equation 1.3 from the CAM. We will call this apparent increased emittance the correlated emittance, ε_{cor} . Other references have termed this the effective emittance [7, 13, 14]. It is the emittance that would be measured if the emittance was to be measured as normal with a non-magnetized beam. However, if one were to remove the correlation between the x and y' space and the x' and y space, then the resulting measurement would show no apparent kinetic angular momentum in the beam. This would be the uncorrelated emittance, ε_u , sometimes referred to as thermal emittance.

The eigen emittances are the maximum and minimum possible values for emittance. Solving for the eigen emittances via the Σ matrix values can be done by solving for the following equation

$$\det(J\Sigma - i\varepsilon_{\pm}I) = 0 \quad (2.7)$$

where J is the symplectic matrix

$$J = \begin{bmatrix} 0 & 1 & 0 & 0 \\ -1 & 0 & 0 & 0 \\ 0 & 0 & 0 & 1 \\ 0 & 0 & -1 & 0 \end{bmatrix} \quad (2.8)$$

Σ is the second order moments of the transverse beam distribution, as displayed in 2.1, and I is the identity matrix [15].

We can calculate for the eigen emittances from the magnetization and the uncorrelated emittance via [13]

$$\varepsilon_{\pm} = \sqrt{\varepsilon_u^2 + \mathcal{L}^2} \pm \mathcal{L} \quad (2.9)$$

So it can be seen given a \mathcal{L} there will be a significant difference between the eigen emittances. Also notice that as the magnetization \mathcal{L} vanishes the eigen emittances turn into the same value, $\varepsilon_+ = \varepsilon_- = \varepsilon_u$.

These expressions can be further simplified in the case of $\mathcal{L} \gg \varepsilon_u$ we can simplify to [16]

$$\varepsilon_+ = 2\mathcal{L} \quad \text{and} \quad \varepsilon_- = \frac{\varepsilon_u^2}{2\mathcal{L}} \quad (2.10)$$

The relations of these equations are plotted in fig. 2.3 for reference of shape and fidelity of the high magnetization assumptions.

Also because there are two variables and two equations this can be solved in the other direction too.

$$\varepsilon_u = \sqrt{\varepsilon_+ \varepsilon_-} \quad (2.11)$$

$$\mathcal{L} = \frac{\varepsilon_+ - \varepsilon_-}{2} \quad (2.12)$$

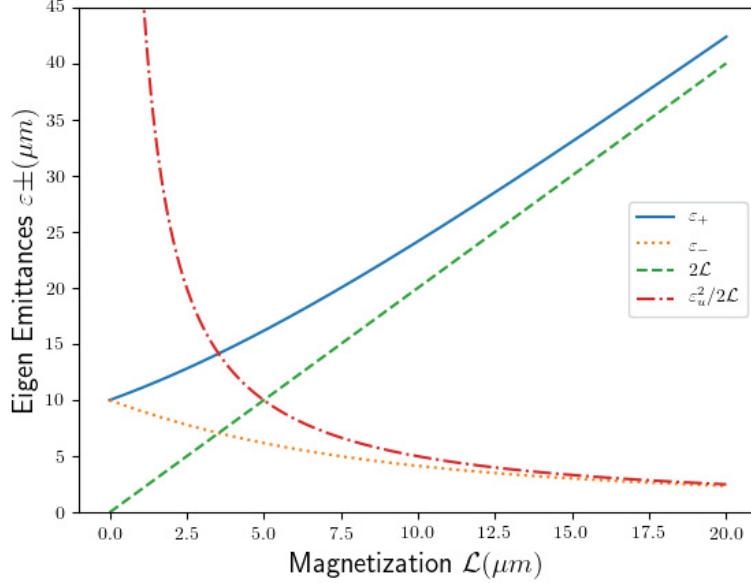


Figure 2.3: An example of the partition of eigen emittances from Eq. 2.9 with the accompanying high magnetization assumptions. An uncorrelated emittance of $10 \mu m$ has been used for demonstration.

2.2.2 Emittance Measurements of Magnetized Beams

Because of the cylindrical symmetry associated with beam physics one can use multiple basis of coordinates to describe the beam distribution and the emittances as done in [8]. The most common basis to measure emittances in beam physics is the Cartesian coordinates because of the convenience to measure in experiments. Another alternative is the eigen emittances basis. The convention of eigen emittances only plays a part when there is CAM in the beam, otherwise the eigen emittances are the same as the uncorrelated emittance. However because it describes the maximum and minimum emittances possible of the beam it makes for a good description of the beam emittance extremes.

In the case of magnetized beams there are two basic methods that are used for measuring emittances: correlated, ε_{cor} , and uncorrelated, ε_u , emittances (sometimes called effective and

thermal) and eigen emittances (ε_{\pm}). The case of the correlated and uncorrelated emittances are measuring a magnetized beams emittances in the traditional x and y Cartesian coordinates with the x, y' correlation included and subtracted respectfully. They have the following relation to magnetization \mathcal{L} and each other [13].

$$\varepsilon_{cor} = \sqrt{\varepsilon_u^2 + \mathcal{L}^2} \quad (2.13)$$

$$(2.14)$$

The other basis of measurement is by eigen emittances. Methods of measurement still require the use of the Cartesian emittance slit measurement apparatus's as well as three skew quadrupoles for one method of measurement. The idea is to remove the kinetic angular momentum with the torque of some quadrupole and we use skew quadrupoles so that the final projection is made in the accustomed x and y space [7].

CHAPTER 3

SIMULATIONS OF MAGNETIZED BEAMS

3.1 Simulation Software

Simulations for the electron beam from the photo cathode were primarily done using Impact-T [17]. Impact-T is a particle in cell (PIC) based simulation code that uses time as the variable that it integrates. It has good fidelity of simulations and experiment characteristics, specifically when applying space charge effects in simulations. Other simulation software's that were used include Impact-Z and ELEGANT [18]. Both of these are capable of simulating higher energy electron beams with faster compute times but have less accuracy in space charge effects than a PIC based codes such as Impact-T.

For this set of studies we simulated the injector and acceleration of the beam up to 34 MeV to 8 meters from the photo-cathode, see fig. 3.1 for a schematic of the FAST beam line. After the 8 meter mark, the distribution simulated up to this location can be further simulated in Impact-T or be used as an input distribution for Impact-Z or ELEGANT for faster beam dynamic simulations.

To be able to transition between each code, a script was created to simulate various accelerator setting conditions in all three simulation softwares. The initial purpose of this capability was to simulate the same accelerator conditions across simulation softwares to benchmark to the programs. Another purpose was if the simulations had similar agreement to use the fastest simulation software to do many simulation studies faster. Because there would need to be many simulation studies completed it was valuable to complete a script to

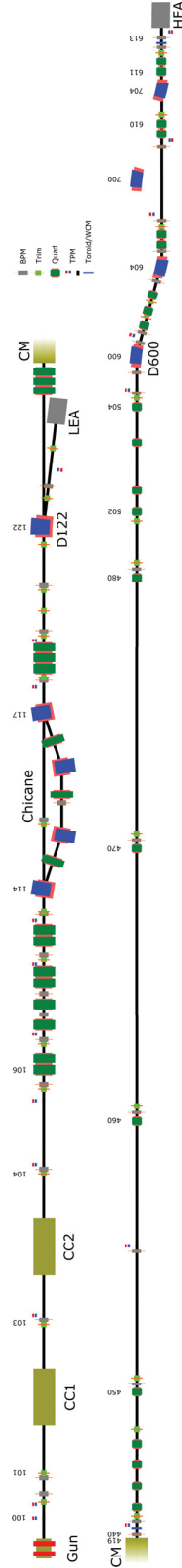


Figure 3.1: The whole linear portion of the accelerator beam line at FAST. There is also an exit for electrons to be shot into the Integrable Optics Test Accelerator (IOTA) just downstream from the blue dipole labeled D604

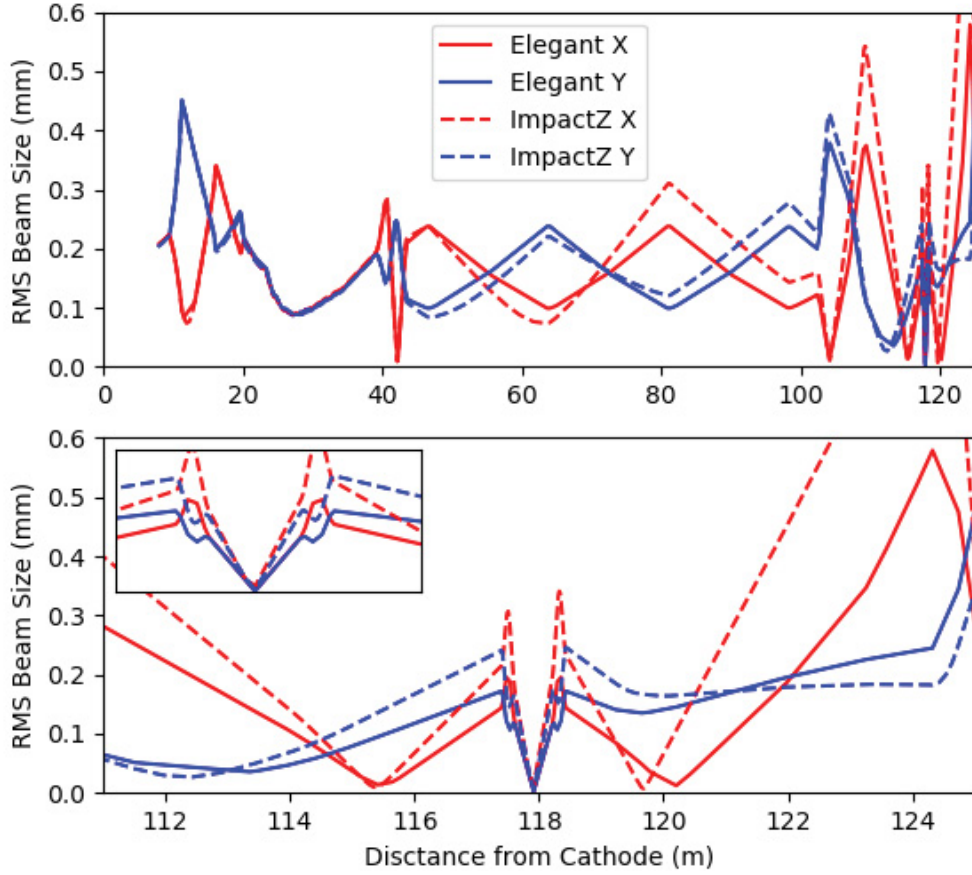


Figure 3.2: Evolution of beam size in the FAST accelerator. Simulated using Imapact-Z and ELEGANT. This offered verification between the two simulation software's and was used later for other comparison studies as well.

transition from one simulation code to the next. Two examples of the simulation softwares being compared is given in figs. 3.2 and 3.5.

3.2 Input Beam Distributions

The simulation studies used two different input distributions. One was a round uniform density transverse distribution with a radius of 2.3 mm. This was primarily used for studying

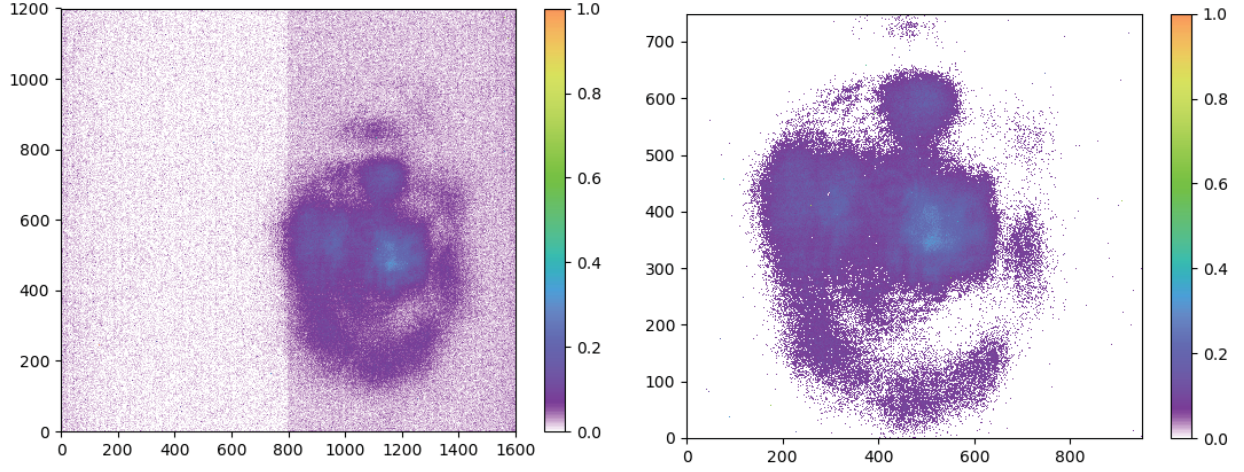


Figure 3.3: Virtual cathode image (left) and corresponding Monte-Carlo generated macro-particle distribution (right).

space charge effects while varying the amount of charge in the simulated beam. Results from this study are included in section 3.4.

The other input distribution used was a realistic distribution created using a Monte-Carlo algorithm. The algorithm uses an image of a distribution as an input and returns a randomly filled discrete distribution that mimics the intensity shape of the input image. An example of a Monte-Carlo distribution used is shown in fig. 3.3. The discrete set of randomly generated points from the image can then be used as a macro-particle transverse input distribution for beam diagnostic simulations. The image used was from the experimental laser distribution on the cathode called a virtual cathode. The virtual cathode gives the laser distribution on the photo-cathode. It corresponds to the initial transverse distribution of the emitted electrons. Radiation from quantum efficiency of electrons being released is not considered in this study. This distribution was used to simulate measurements that can were compared to the experimental results.

3.3 Measuring the eigen-emittances

3.3.1 Mapping technique using round-to-flat beam transformer

To be able to measure the eigen-emittances using the round-to-flat beam transformer (RFBT) we first have to make a flat beam. This is done by using skew quadrupoles that make a net torque on the CAM beam to remove the angular momentum. As noted in [7], the first quadrupole magnet introduces an asymmetry in the $x - y$ space, and then the other two quadrupole magnets downstream are tuned so that there is a torque that cancels out the angular momentum of the beam. A simple formulation to compute the quadrupole magnets settings is described in [12] and also applied and demonstrated in [19]. Recently experiments at the Argonne Wakefield Accelerator (AWA) demonstrated the mapping of eigen-emittances into conventional emittances resulting in a transverse emittance ratio close to 200 [20].

The skew quadrupole settings depend on the relative distances of each of the quadrupoles from each other and the initial beam settings as it enters the first quadrupole. The initial beam settings are set by using the simplified covariant matrix S described as

$$S = \begin{pmatrix} \alpha & \beta \\ -\gamma & -\alpha \end{pmatrix} \quad (3.1)$$

where β is the beta function and $\alpha = d\beta/dz$ associated with the incoming cylindrical-symmetric beam. Using the matrix S as the basis for the initial beam settings and with the

spacing of the quadrupoles of $d2$, $d3$ and dt as the sum of the two spaces between Q1-Q2, Q2-Q3 we can then summarize the quad strength settings required as [12]

$$q_1 = \pm \sqrt{\frac{-d_2(d_t S_{21} + S_{11}) + d_t S_{22} + S_{12}}{d_2 d_t S_{12}}} \quad (3.2)$$

$$q_2 = \frac{(d_2 + d_3)(q_1 - S_{21}) - S_{11}}{d_3(d_2 q_1 S_{11} - 1)} \quad (3.3)$$

$$q_3 = \frac{d_2(q_2 - q_1 q_2 S_{12}) - S_{22}}{d_2(d_3 q_2 S_{22} + q_1 S_{12} - 1) + d_3(S_{12}(q_1 + q_2) - 1)} \quad (3.4)$$

This method uses the thin lens approximation for the quadrupole magnets and is a great starting point for simulation optimizations as it can be easily calculated. However, because the thin lens approximation is valid when $f \gg L$ (when the focal length is much longer than the length of the focusing magnet length) this method can not be relied upon for every case of round to flat beam quad settings calculation. The thin lens approximation does provide a great starting point for optimizing quad settings in simulations. Another method developed in [20] is the use of a thick lens optimization method which was also used in some of these studies and showed further agreement with simulation optimizations in Impact-T. Simulations of the round to flat beam transformation are illustrated in Fig. 3.4 using Impact-T.

Impact-T was primarily used in the early regions of beam dynamic simulations up to 8 meters downstream from the photocathode. This is the region of the accelerator where the energy of the beam is lower than 34 MeV. This means that the beam is less ridged as it travels through this section and more susceptible to space charge effect aberrations. Once the beam is more ridged at the 8 meter mark Impact-T is able to save the distribution at 8 meters to then be converted and used in all three simulations codes. This allows for clarification that whatever we do in the skew quads is agreed upon by multiple simulation codes.

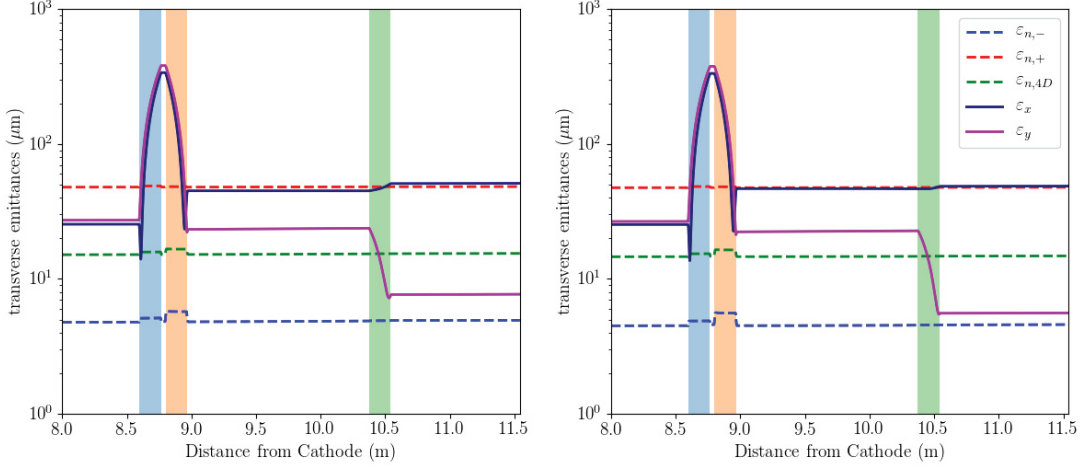


Figure 3.4: Evolution of eigen, conventional and 4D emittances along a RFBT section for the two possible solutions. The color bars represent the positions and lengths of the skew quadrupoles that form the RFBT.

In the end the ELEGANT built-in optimizer was used to minimize the beam size in the x direction and maximize the beam size in the y direction. A comparisons between ELEGANT, Impact-Z and Impact-T simulations of a flat beam is shown in fig. 3.5. It confirms the three beam-dynamics programs are in reasonable agreement at 34 MeV for the maximum bunch charge considered in our experiment (3.2 nC).

3.3.2 Measurement using the Scanning Slit Technique

The other main method of measuring magnetization is by using traditional methods of measuring emittance: using emittance slits. This method consists of using a thin metal slide with a small slit in which to allow a small portion of the beam to pass through to continue propagating. For instance, the slits used at the FAST low energy beam line are laser machined in a 0.5-mm thick tungsten plate and have a size of $40 \mu\text{m} \times 12.7 \text{ mm}$. The beamlet

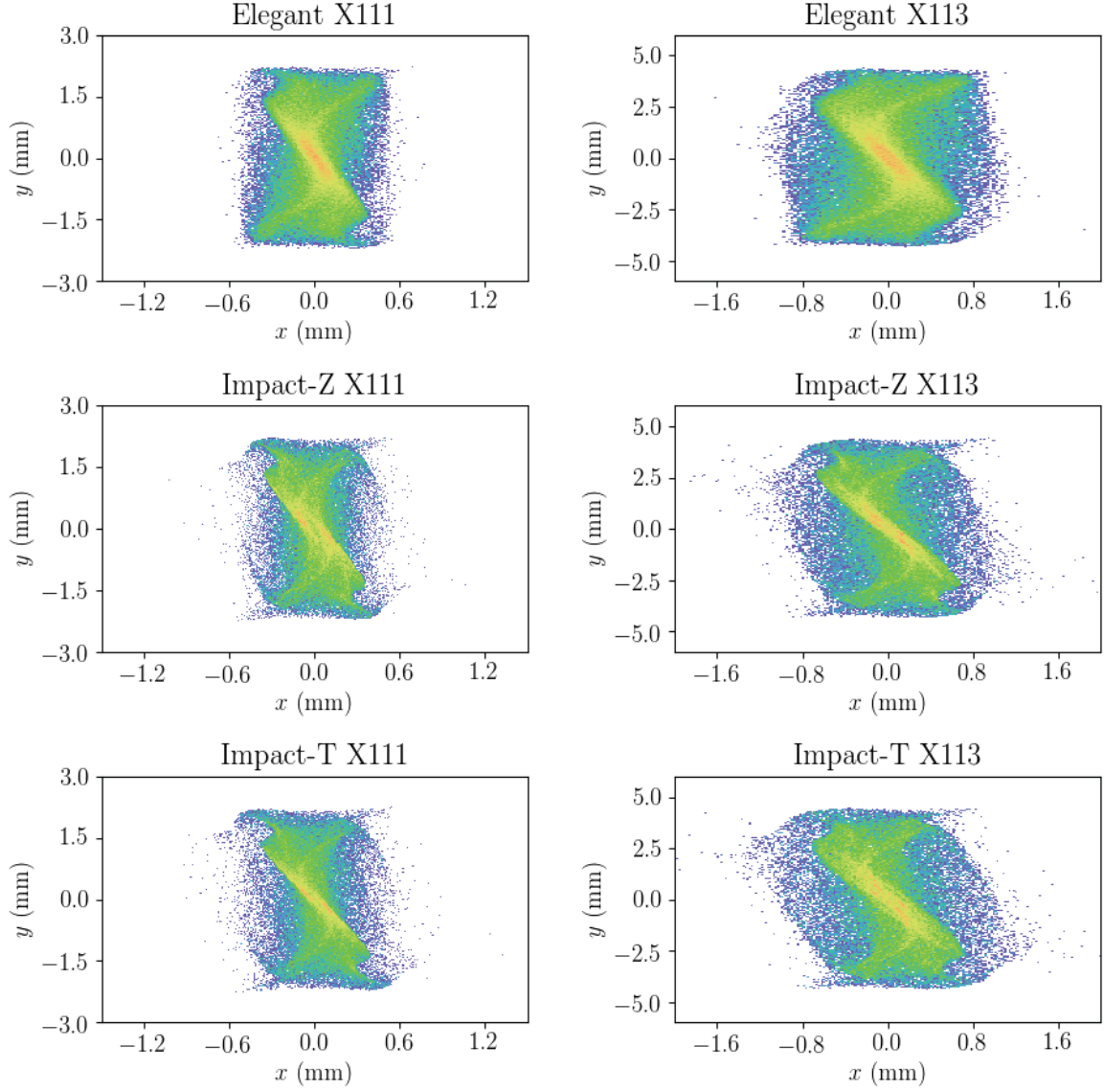


Figure 3.5: Transverse distribution simulated with Elegant, Impact-T and Impact-Z. Simulations of a magnetized beam at observation points X111 and X113 (positioned at 10.54 and 11.35 meters away from the photo-cathode injector).

generated by the slit is observed on a Ce:YAG scintillating screen located downstream of the slits. A CCD camera is used to record the beam distribution on the Ce:YAG surface.

Nominally, the electron beam does not have any magnetization for this method of emittance measurement. Thus the transverse size of the resulting viewed slit provides a measurement of the beamlets divergence relating to the $\langle x' \rangle$ in eq. 1.3. Scanning the slits through the beam provides a means to measure the beam emittance and possibly the phase-space distribution. In the presence of magnetization the slit image on the Ce:YAG screen is sheared due to the angular momentum. The corresponding tilt angle, or shearing angle, can therefore be used to infer the angular momentum [11].

The method also gives a way to measure two types of emittances: the correlated emittance, ε_{cor} , and the uncorrelated emittance, ε_u . The correlated emittance is the emittance that would be measured if the appropriate projections from the pictures were made without any alteration of the data. The uncorrelated emittance is the measured emittance if the raw data is turned the number of degrees that would need to be to get the smallest projected beam slit size. This can be looked at as removing the tilt. Removing the tilt resulting from the shearing on the beamlet image can be understood as effectively removing the contribution from the angular momentum from the beam and thus measuring only the conventional emittance.

Using the convention from Ref. [13] we can use Eq. 2.13 to relate the magnetization \mathcal{L} to the correlated and uncorrelated emittances

$$\mathcal{L} = \sqrt{\varepsilon_{eff}^2 - \varepsilon_{th}^2}. \quad (3.5)$$

Therefore the magnetization \mathcal{L} can be inferred from a measurement of the correlated and uncorrelated emittances.

A simulation that would mimic the set up of the experiment proposed and give expectations for the expected results was made. Because we were also working with simulations we could computationally calculate what the values of magnetization, by a direct measurement of magnetization using Eq. 2.3. The simulation studies for this practical experiment were done using a combination of ELEGANT distribution data files and python scripting. An example of the resulting plots that were used to visualize the data is shown in Fig. 3.6.

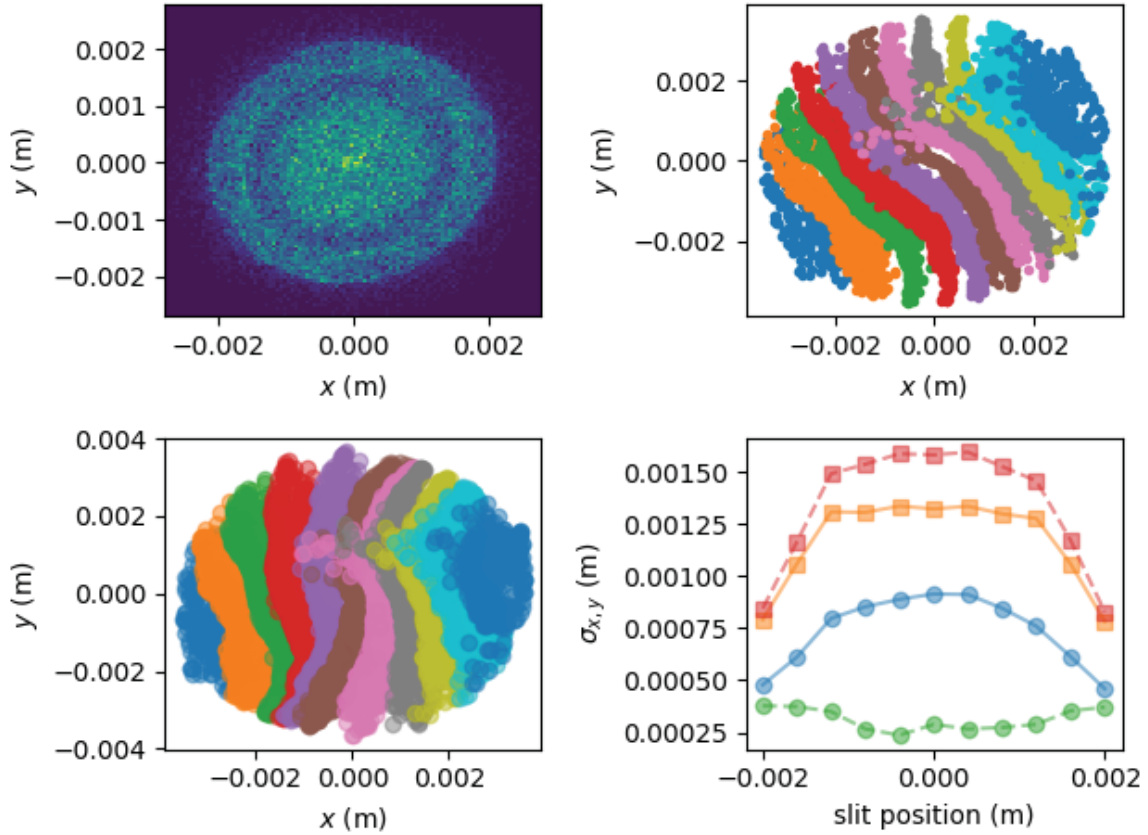


Figure 3.6: Sample of simulating the slits emittance experiment for the LDRD experiment down stream of the cryo-module at FAST. Top left is a x-y space density plot with top right being a simulation of 11 evenly spaced positioned slits and letting the macro particles be transported through a drift space of 2 meters. The bottom left shows those same particles but just turned so that the beams effective beam size projection is decreased. Bottom right is the beam sizes for each of the x and y directions.

3.4 Observation of Peripheral Halo Formation

While exploring how space charge affected a magnetized beam, apparent space charge induced rings would appear in simulations. These rings were particularly evident when simulating with the uniform distribution. Further investigated was inconclusive of what the exact process is that created them. We were able to successfully identify that this happens when there is magnetization and high space charge effects happening in our simulations. Understanding how this halo formation happens, if it can be seen in experiments and if it can be mitigated will be of interest for having optimal cooling performance.

Studies investigating this included simulations in Impact-T with varying beam charge and particle number simulations. Because Impact-T uses a PIC computational method we used a standard density of at least 5 macroparticles per cell in the mesh grid of the PIC system. Keeping the magnetization constant at $18 \mu m$ by the method of measurement of magnetization described in Eq. 2.3. In the cases of radial distributions graphed in Fig. 3.7, the space charge algorithm was setup with a 32^3 grid and 200,000 macro particles were used while varying the amount of charge in a beam considered.

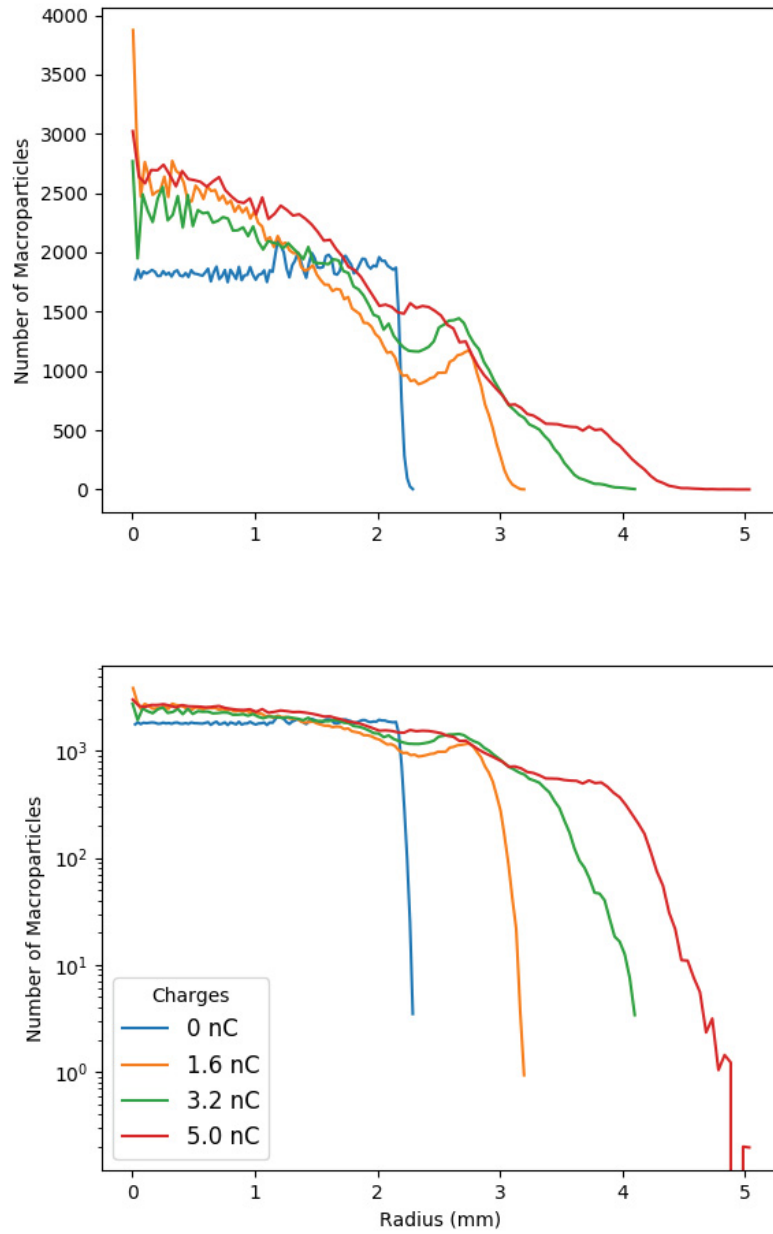


Figure 3.7: Radial distribution of the charge in a linear plot (top) and logarithmic (bottom) plots.

CHAPTER 4

EXPERIMENTS AT THE FAST FACILITY

4.1 Experimental Setup

A schematic of the FAST facility injector beam-line appears in Fig. 4.1. The electron source consists of a 1+1/2-cell RF gun with a Cs₂Te cathode. The RF gun is followed by two superconducting accelerating cavities (CAV1 and CAV2). Further downstream, the beamline includes quadrupole magnets, a bunch compressor chicane (BC1), and a low energy dump (LE absorber). There is also a spectrometer located just upstream of the LE absorber. The available diagnostics are labeled as “X” in Fig. 4.1. Downstream of the photoinjector, a long accelerating cryomodule accelerated the beam up to 300 MeV for further experiment or injection in the Integrated Optics Test Accelerator (IOTA) storage ring (at 100-150 MeV).

The diagnostics include beam position monitors (BPMs) that provide the beam position (center) in the x and y directions relative to the center of the beamline, and transverse profile monitors (TPMs) which consists of Ce:YAG (cerium-doped yttrium aluminum garnet) scintillating screens that allow for the transverse electron beam density to be measured using CCD cameras. Some of the diagnostics stations include single- and multi-slit diagnostic screens for x and y directions with $40\pm 5\ \mu\text{m}$ wide and 12.8-mm tall slit openings. These latter stations are used to measure the emittances of an electron beam.

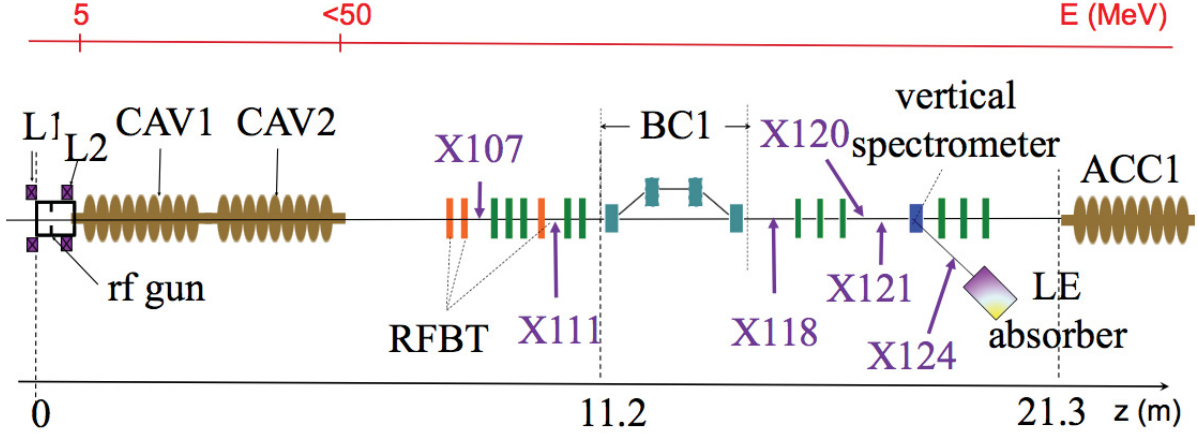


Figure 4.1: The Fermilab Accelerator Science and Technology (FSAT) facilities electron beam injector. Each of the purple labels of X... includes a Transverse Profile Monitor (TPM) allowing for pictures of the transverse beam shape to be taken at these locations. The Green rectangles represent quadrupoles that are used for focusing the electron beam. The three orange rectangles, labeled RFBT, are skew quadrupoles (quadrupoles axially turned 45 degrees). These allow for a magnetized electron beam to be transformed into a flat beam.

4.2 Measurement Methods and Analysis

There are two methods used in this study to measure the eigen emittances of an CAM dominated beam: mapping the eigen emittances to the x and y planes with a Round to Flat Beam Transformation [13], and calculation of the eigen emittances from the measured correlated and uncorrelated emittances using traditional slits. Both methods are explained and elaborated on how they were used in experiments in this chapter. The magnetization calculation from the cathode settings was also used to compare against the measurements of the electron beam in both methods of measurement and is explained in the next section.

4.2.1 Magnetization at the Cathode

The measurement of a beams magnetization can be measured directly in a couple of ways. First, recall that the magnetization for a beam is determined by the magnetic field on the cathode in the manor of equations 2.5 and 2.6. In the experiments, the following relation of the magnetic field on the photo-cathode obtained from the solenoid settings were able to calculate for the magnetic field on the cathode

$$B_c(I_B, I_M) = -4.1114I_B + 0.9768I_M \quad (4.1)$$

where B_c is the magnetic field on the cathode in units of Gauss with I_B and I_M as the solenoid currents in Amps for the bucking and main solenoid magnets at the photo-cathode. This equation is a best fit from experimental data taken when the photo-cathode was being commissioned [21]. A plot of the relative magnetic field is given in Fig. 4.2.

The RMS spot size of the laser on the cathode for Eq. 2.6 was obtained from using a virtual cathode camera image. A calibration of $9.2 \mu m$ per pixel was provided and used with considerations for the optical alignment set up for this camera. By using the virtual cathode image discussed in section 3.2 we can calculate the transverse beam size of beam, σ_c . An example of the virtual cathode image analysis can be seen in Fig. 4.3.

This is one method of calculating the magnetization experimentally with input from the bucking and main solenoid currents and the sigma spot size at the cathode from the laser. This method is used to compare to the other two methods of measurement.

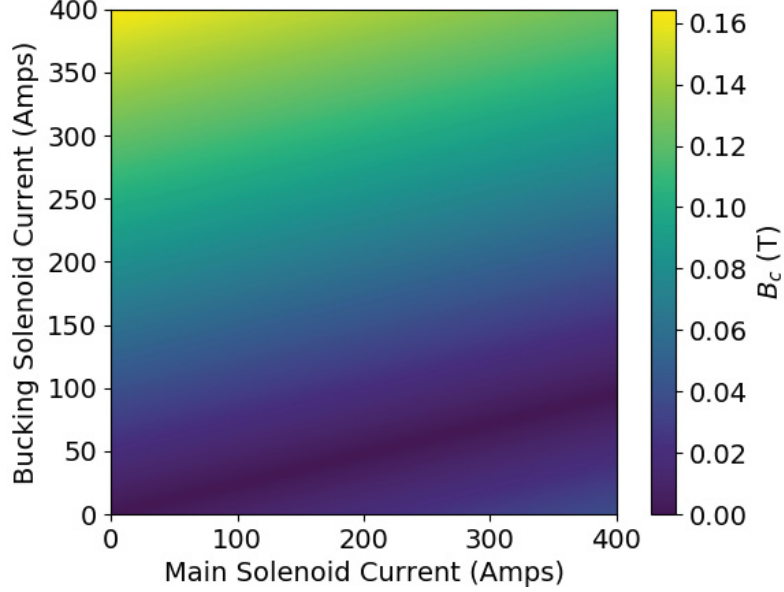


Figure 4.2: Contour plot of the magnetic field on the cathode as a function of the main and bucking solenoid currents.

4.2.2 Round to Flat Beam Transformation Method

The RFBT measurement method takes advantage of the kinetic angular momentum intrinsic to a magnetized beam and maps the eigen emittances to the conventional x and y emittances [7]. This is done using a set of three skew quadrupole magnets each separated by a known drift space length. A skew quadrupole is mechanically the same as a regular quadrupole but the configuration of the magnet is such that the magnetic fields are turned axially by 45 degrees. The first skew quadrupole magnet puts an asymmetrical correlation in the x-y space while the other two skew quadrupoles are tuned to use the asymmetry to cancel out the angular momentum. Using skew quadrupoles allows for the final beam to be mapped into the x and y planes. If regularly aligned quadrupoles were used the transformation would make a 45 degree tilted flat beam.

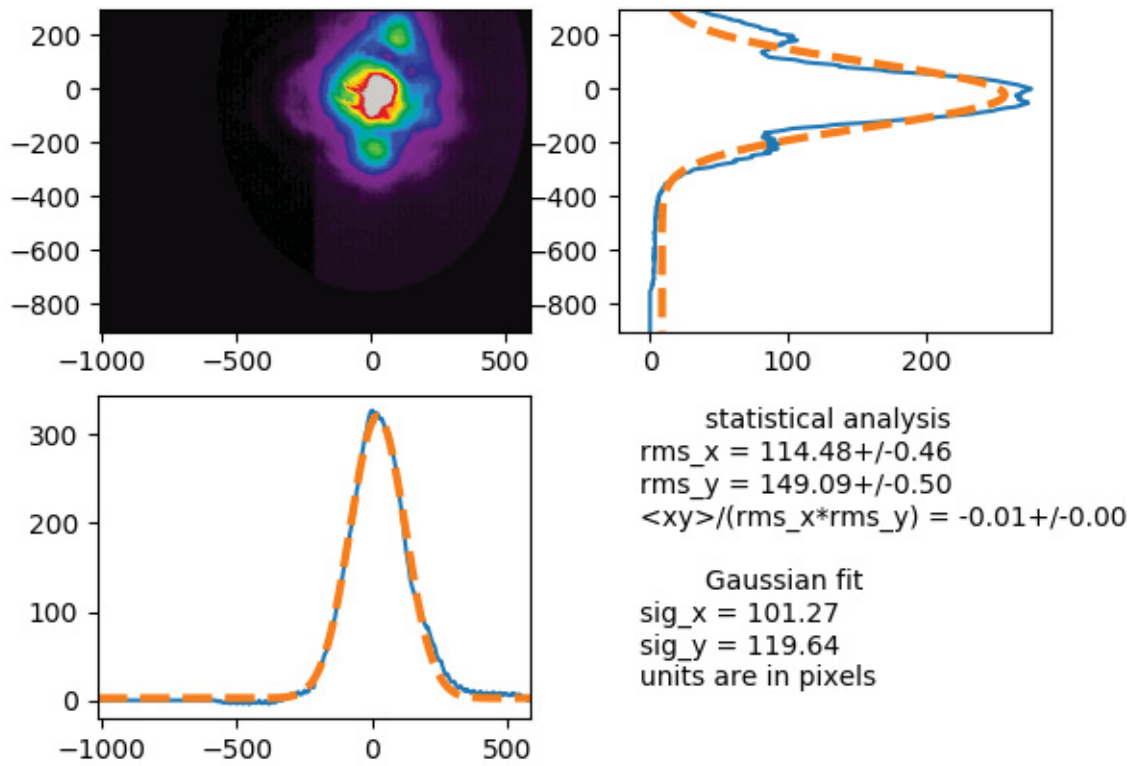


Figure 4.3: Example of virtual cathode Image analysis for measurement of the beam sigma size. This is used as a reference for measurements of the electron beam dynamic magnetization's.

The settings the skew quadrupoles magnets need to have to make a flat beam depend greatly on the initial beam dynamics at the entrance of the RFBT section and the drift space lengths between the skew-quadrupoles. A summary of making the RFBT transformation was discussed in section 3.3.1. One specific requirement for the conversion of the flat beam is to ensure that the beam is at a waist upon entering the first skew quadrupole. Being at a waist means that the transverse size of the beam is at a minimum. This allows for the predominate direction of travel in the transverse direction to be predominantly in the radial direction with the kinetic angular momentum. The needed skew quadrupole setting dependencies on the initial beam conditions are well documented [19, 13, 7].

It should also be mentioned how the quadrupole strength is measured. Similarly to how an optical lens has a focal length, a focusing quadrupole magnet also has a focusing length. However it only focuses in one of the two transverse directions, x or y. The other direction is unfocused, or, it could be said, has a negative focal length. The quadrupole focal length can be written as

$$\frac{1}{f} = KL = \frac{B'L}{B\rho} \quad (4.2)$$

where f is the focal length, K is the geometric focusing strength of the quadrupole, L is the effective length of the quadrupole, B' is the gradient of the quadrupole magnet and $B\rho$ is a term called the beams magnetic rigidity. The rigidity is a quality used to describe the resistance of a beam to turn under an amount of magnetic field. As the magnetic field increases the radius of curvature will decrease making the whole term $B\rho$ be a constant that measures the relationship of the beams momentum or energy and the amount of focusing strength the beam would need to be focused.

This method of measuring eigen emittances and magnetization was attempted in both runs of experiments and was successful in run 1. The specifics of the data collected on this method are described in section 4.3.1.

4.2.3 Magnetization from Beam Slit Measurements

The equations used for measuring experimental emittance is as follows

$$\varepsilon = \sigma_{X118} \frac{1}{L\omega_T} \sum_i^N \omega_i \sigma_i \quad (4.3)$$

where σ_{X118} is the beam spot size at the X118 slit screen, L is the distance from the slit screen to the viewing screen, ω_i is the i th data point intensity at the viewing screen, N is the number of slits in a given data collection, and σ_i is the i th beam size as projected in the direction of emittance measurement. Also ω_T is the sum total intensity of the measured slits.

The error of the measurement taken by considering the differentiation of the emittance measurement errors of the beam spot size, σ_{X118} , and the beam divergence as projected to the appropriate axis is taken as

$$d\varepsilon = \sigma_{X118} \frac{d\sigma_i}{L} + d\sigma_{X118} \frac{1}{L\omega_T} \sum_i^N \omega_i \sigma_i \quad (4.4)$$

where the product rule has been applied for the two beam dynamic measurable variables. The $d\sigma_{X118}$ term is calculated from the variation of the beam size from the three pictures taken in each run and the $d\sigma_i$ term is taken to be the standard deviation of the measured slits sizes for all of the slits.

This method of emittance measurement can be traced back to the definition of emittance used in Eq. 1.3. We can say that if there is a correlated and an uncorrelated portion of the beam between the position and the divergence then

$$x' = \tilde{x}' + \alpha x \quad (4.5)$$

where the \tilde{x}' is representative of the uncorrelated divergence and α is related to the courant-snyder parameter alpha [22]. We then have a representation for $\langle x'^2 \rangle$ in terms of the random variable

$$\langle x'^2 \rangle = \langle \tilde{x}'^2 \rangle + \alpha^2 \langle x^2 \rangle \quad (4.6)$$

and then we can also apply this substitution into $\langle xx' \rangle^2$ and get

$$\begin{aligned} \langle xx' \rangle^2 &= \langle x(\tilde{x}' + \alpha x) \rangle \\ \langle xx' \rangle^2 &= \langle x\tilde{x}' \rangle + \alpha \langle x^2 \rangle \\ \langle xx' \rangle^2 &= \alpha \langle x^2 \rangle \end{aligned} \quad (4.7)$$

Now substituting equations 4.6 and 4.7 into the definition of emittance, Eq. 1.3 results with

$$\begin{aligned} \varepsilon^2 &= \langle x^2 \rangle \langle (\tilde{x}'^2 + \alpha^2 x^2) \rangle - \alpha^2 \langle x^2 \rangle^2 \\ \varepsilon^2 &= \langle x^2 \rangle \langle \tilde{x}'^2 \rangle + \alpha^2 \langle x^2 \rangle^2 - \alpha^2 \langle x^2 \rangle^2 \\ \varepsilon^2 &= \langle x^2 \rangle \langle \tilde{x}'^2 \rangle \end{aligned} \quad (4.8)$$

Thus we can say that the emittance in 4.8 is an suitable method of experimentally measuring magnetized electron beam emittances. Using this emittance measurement was very useful for experiments performed for this research.

4.3 Experimental Measurements

Presented here are the experimental measurements that were completed for these studies. The RFTB mapping experiment was completed in the first run while the slit measurements were completed in the second run.

4.3.1 RFBT Eigen-Emittance Mapping Experiment

In our first run we had successfully implemented the RTFB transformation method and measurements for a single case. Run 2 efforts were unsuccessful in the first attempt to implement the RTFB in the first attempt and the second attempt was canceled for the Coronavirus. We were able to collect one set of data for the RFBT mapping emittance measurements and we now report on these measurements.

The settings for the magnetization set up are described in table 4.1. The average sigma size on the cathode and average RMS sizes were calculated using the python tool on the virtual cathode images as depicted in fig. 4.3 Using the virtual cathode images we could calculate for a theoretical average magnetization using eq. 2.5 or eq. 2.6. A distribution was also made using the Monte Carlo method as discussed in section 3.2 to make a simulation input data set for simulating the experiments to compare simulation and experimental results. The raw image data used is displayed in Fig. 4.4 for reference.

We used a method of estimating the emittance in the following equation

$$\varepsilon = \sigma_{X118}\sigma_{slit}/d \quad (4.9)$$

Using this method was an easy method for quickly calculating the eigen emittances. In doing this analysis we used the camera pictures to calculate the spot size of the full beam size in the x and y directions and the beam sizes of one slit in the x and y directions for the X120 position of the middle slit.

As can be seen in table 4.1 the measured magnetization can also use the RMS size of the cathode and have good matching agreement. For this case this appears to be more precise, perhaps because the uncertainties were smaller.

Table 4.1: Summary of beam parameters and magnetization measurements of the RTFB emittance measurement data compared to the cathode magnetization measurement data. ε_u is the uncorrelated emittance and \mathcal{L} (exact) uses Eq. 2.9 with the eigen emittances and solves for ε_u and \mathcal{L} .

Beam & Accelerator Settings		
Paramters	units	Value
$I_{Bucking}$	Amps	130 ± 1
I_{Main}	Amps	310 ± 1
$\langle \sigma_{cathode} \rangle$	mm	1.43 ± 0.31
$\langle RMS_{cathode} \rangle$	mm	1.48 ± 0.03
Energy	MeV	$32.436 \pm .001$
Charge	nC	$3.2 \pm .13$
RFTB Eigen-Emittances		
Paramters	units	
ε_+ (measured)	μm	32.5 ± 2.9
ε_- (measured)	μm	2.2 ± 1.9
Uncorelated emit ε_u (calc.)	μm	$8.2 \pm .4$
Magnetization \mathcal{L} (calc.)	μm	15.2 ± 1.5
Cathode Magnetization		
Paramters	units	
Magnetization (σ)	μm	13.9 ± 6
Magnetization (RMS)	μm	14.9 ± 0.6

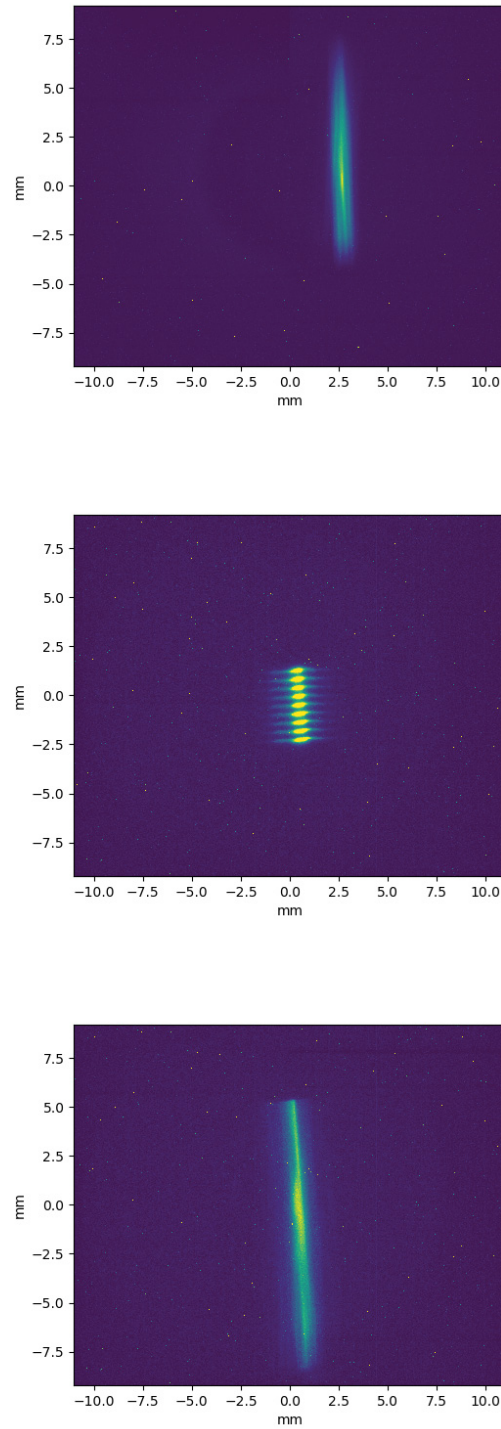


Figure 4.4: RFBT data from Run 1. Flat beam at X118 (top), Horizontal slits measuring the larger emittance (middle) and vertical slits measuring the smaller emittance (bottom).

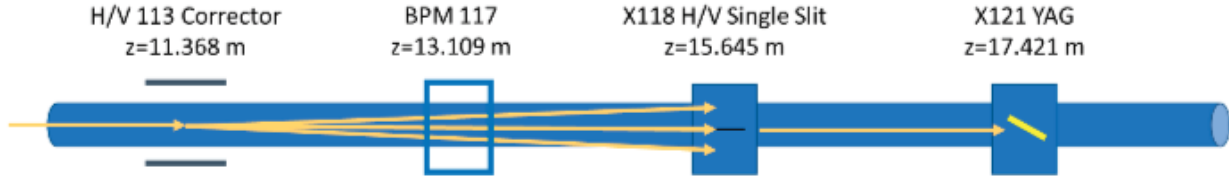


Figure 4.5: Schematic of slit experiment at FAST.

4.3.2 Magnetization from Slit Measurements

Measuring the emittance experimentally from the slits proved to be difficult for the experiment for a couple of reasons. One reason was because of a mechanical failure that prevented us from using the measurement slits in the traditional way. With some creative thinking it was concluded that the best course of action to collect data was to steer the magnetized round beam using some small beam positioning corrector onto a stationary single emittance slit. See Fig. 4.5 for details of the data collection set up.

To minimize induced dispersion, the steering corrector that used was 4.27 meters away from the slit. Seeing as the most the beam was kicked viewed on the slit emittance screen was on the order of 1 cm dispersion was concluded to have little effect for our measurements.

Using this method of scanning the beam over a stationary slit created a challenge in the analysis of the data. Creating a scanning beam over the stationary slit made it so that the while the one side of the beam would be going through the slit, it would be coming out of the slit at an angle that would make that slit appear to be coming out of the opposite side of the screen. This complication is demonstrated in Fig. 4.5.

This made it so that the measurement of the true position would be difficult and while this was attempted the results were not as successful or reliable as hoped. Instead, similar triangles were employed along with the BPM data to show what portion of the beam and

how much intensity coming through the slit to map how much intensity came through at that point. This effort was successful and some example data is shown in fig. 4.7.

Experimentally measuring the magnetization with slit emittance methods was thus successful in the end all things considered. The process that was used to make measurements from the data is described for the remainder of the section.

Data collection included 35 data sets in all. Each data set consisted of 20 iterations of scanned parts of the beam, from left to right or top to bottom. Each iteration of the scan contained 1 background image and three data collection images. With each iteration the BPM data from BPM 117 as shown in Fig. 4.5 was collected as well. The difference in iterations was the strength of the horizontal or vertical corrector dipole strength at the 113 station again referencing to Fig. 4.5. The resulting 3000+ pictures of data were taken and sifted through to make sure there was no corrupted data, of which there were a few found.

For emittance measurement using the equation described in the previous section 4.2.3 we will need each slit's beam size, its smallest "turned" beam size projection and the beam size at X118, σ_{X118} . Each of these components are discussed next.

First was to take the raw data and sift through the background noise for easy projection of pictures onto the x and y axis'. While the data collection included a collection of a background image for every 3 pieces of data collected, there would still be salt and pepper noise from stray electrons exciting the YAG screen. To compensate for this a series of image filters were employed to clean the images including a median filter and a percentage threshold. An example of this filtering is shown in Fig. 4.6.

For most accurate and fastest processing of data, the median filter method was utilized to filter stray noise data. The median filter works by going over each image with a $n \times n$ grid over each section of pixels, where n is an odd number and is provided by the user to define. The median of the values in the grid would be returned as the value for the middle pixel. The effectiveness of the method can be seen between the second row and last row of

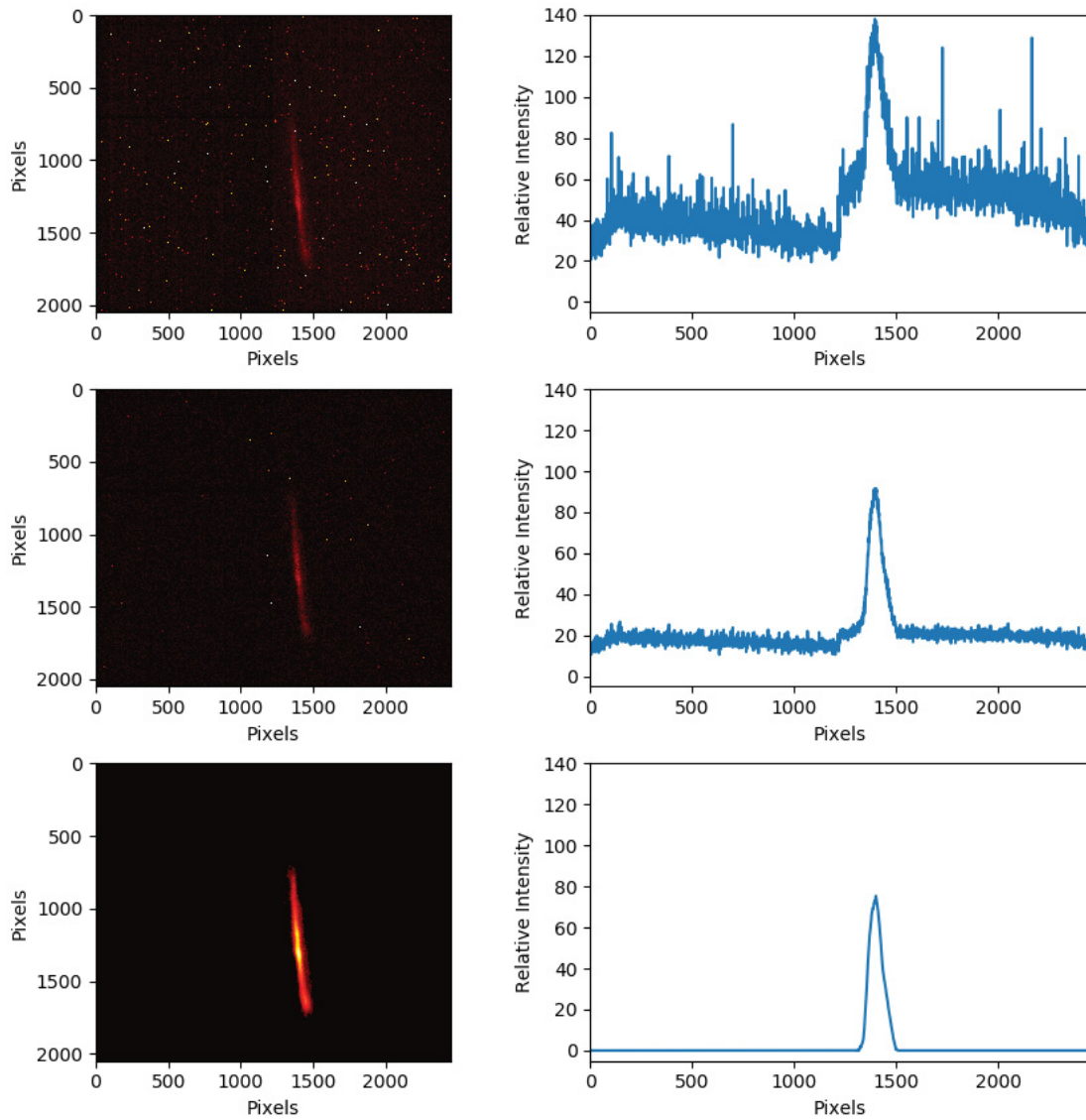


Figure 4.6: Example of image analysis process. Taking the raw data (top row) and subtract the background noise image still resulted in a noisy projection (middle row). Next apply a median filter algorithm and a zeroing threshold for anything less than three percent of the maximum (bottom row).

data in Fig. 4.6. Using the median filter means that analysis of all of the slits can be done faster once the filtered images are all saved separately.

Another process that needed to be developed was method to find the angle of the slits, or an angle finder. To be able to measure the uncorrelated emittance (or thermal emittance) the image would need to be turned so that the standard deviation of the projection would be minimized. The python package `scipy.ndimage` has a `rotate` function that was used to turn images for the purpose of having a good quality default image processing interpolation of up to 3rd order. With this accuracy of image rotating the angle of an images slit could be found with 0.01 degrees of angle in a turn.

Emittance measurements lastly required knowing the beam size of the beam at X118, σ_{X118} as shown in Eq. 4.3. This was accomplished by using the BPM data from BPM 117. The BPM records the relative position of the of highest charge in micrometers and was tuned to give reliable measurements of where the centroid of the beam would be in the x and y directions. This gives a similar triangle that can be used to calculate for the relative position of the resulting beam that is shown in the camera for a larger apparent beam size measurement. Further more to gauge the amount of intensity that was coming through at that relative position, the iterations picture would be integrated over to get the intensity of the beam at that relative position at X118. This was used then as the y axis for the beam size measurement at X118. An example of some data from the BPM and the intensity data are shown in Fig. 4.7.

Next it was a matter of calculating for the magnetization and then calculating for the eigen emittance values. This can be done by using the already calculated correlated and uncorrelated emittances by the relation from Eq. 2.9 where the ε_{cor} is the correlated emittance

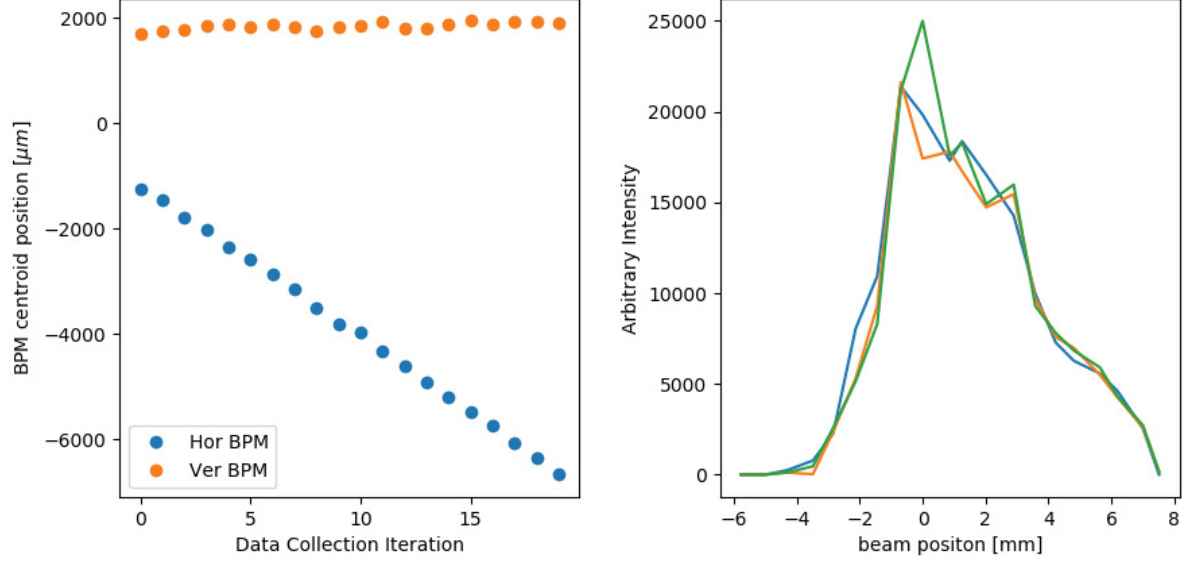


Figure 4.7: Example of data for the BPM data in the x and y directions and the intensities at the relative positions calculated from similar triangles from the BPM data. there are three data lines for each of the iterations of data collection.

and ε_u is the uncorrelated emittance. Using Eq. 2.13 we can solve for the magnetization in terms of measurements that we can make as such.

$$\mathcal{L} = \sqrt{\varepsilon_{cor}^2 - \varepsilon_{unc}^2} \quad (4.10)$$

Experimentally this is how magnetization is calculated from the electron beam emittance measurements. Using this, there is also a simplification with the measurements to calculate for eigen emittances. Because \mathcal{L} uses the uncorrelated emittance as in Eq. 4.10, the eigen emittances can then be written as

$$\varepsilon_{\pm} = \sqrt{\varepsilon_{unc}^2 + \mathcal{L}^2} \pm \mathcal{L} \quad (4.11)$$

$$\varepsilon_{\pm} = \varepsilon_{cor} \pm \mathcal{L} \quad (4.12)$$

4.4 Comparison of Theory, Simulations and Experiments

Our task was to show that the eigen emittances can meet the required parameters for a possible application of electron cooling at an EIC. The requirements that we were aiming to show is an eigen plus emittance, ε_+ or drift emittance of $36 \mu m$ and a maximum of $19 \mu m$ eigen minus emittance, ε_- or cyclotron emittance. The data collected that varied specifically the magnetization is shown in Figs. 4.8 through 4.11.

The specified challenge was to show with the data that has been collected with the two methods of showing the emittance, that these expectations of the cooling electron beam is achievable. As far as the eigen emittances go, they do meet the specifications for staying below the required $19 \mu m$ of cyclotron emittance. The drift emittance can then be matched for the required eigen plus emittance as required. The x and y directions are geometrically averaged by square rooting the product of the x and y eigen emittances calculated from one magnetization for the same solenoid settings.

The fit line that can be observed from plots 4.8-4.11 are made using the geometrical average of the x and y direction measured eigen emittances such that

$$\varepsilon_{avg} = \sqrt{\varepsilon_{\pm,x} \varepsilon_{\pm,y}} \quad (4.13)$$

This was done to minimize effects of asymmetry on measurements. These four averaged data points were used for a data fit using a least squares fit to Eq. 2.9. The yellow space indicates the error of the least square fit parameter from python's scipy optimize routine. The simulation data shown was completed using Impact-T and simulating the main solenoid at 330 Amps (which is consistent with all the data points displayed here) and varying the bucking solenoid from 75 Amps to 350 Amps.

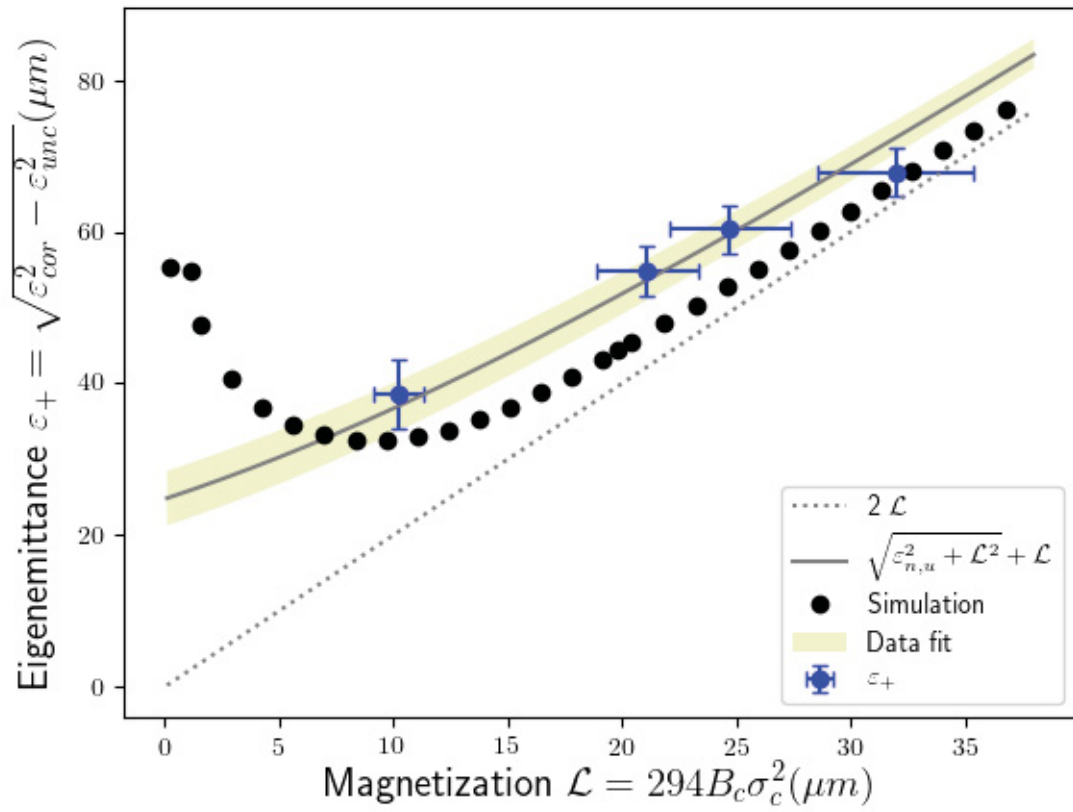


Figure 4.8: Eigen emittance plus experimental data plotted against the calculated magnetization for the 3.2 nC case

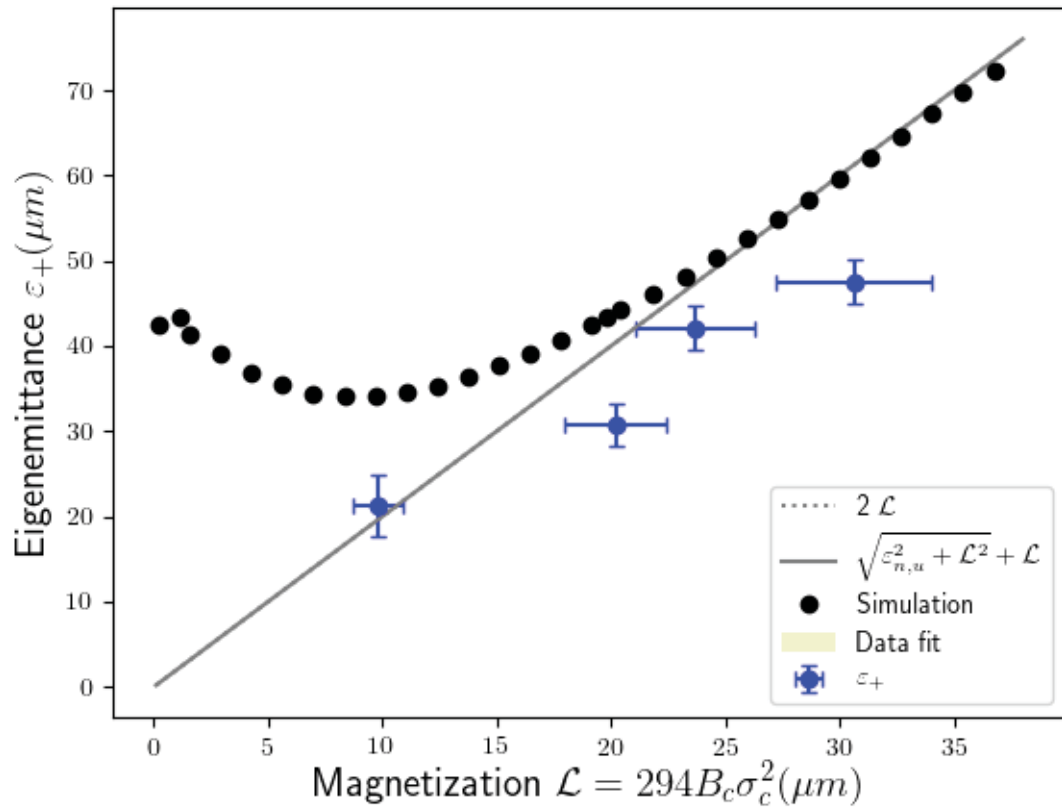


Figure 4.9: Eigen emittance plus experimental data plotted against the calculated magnetization for the 1.6 nC case

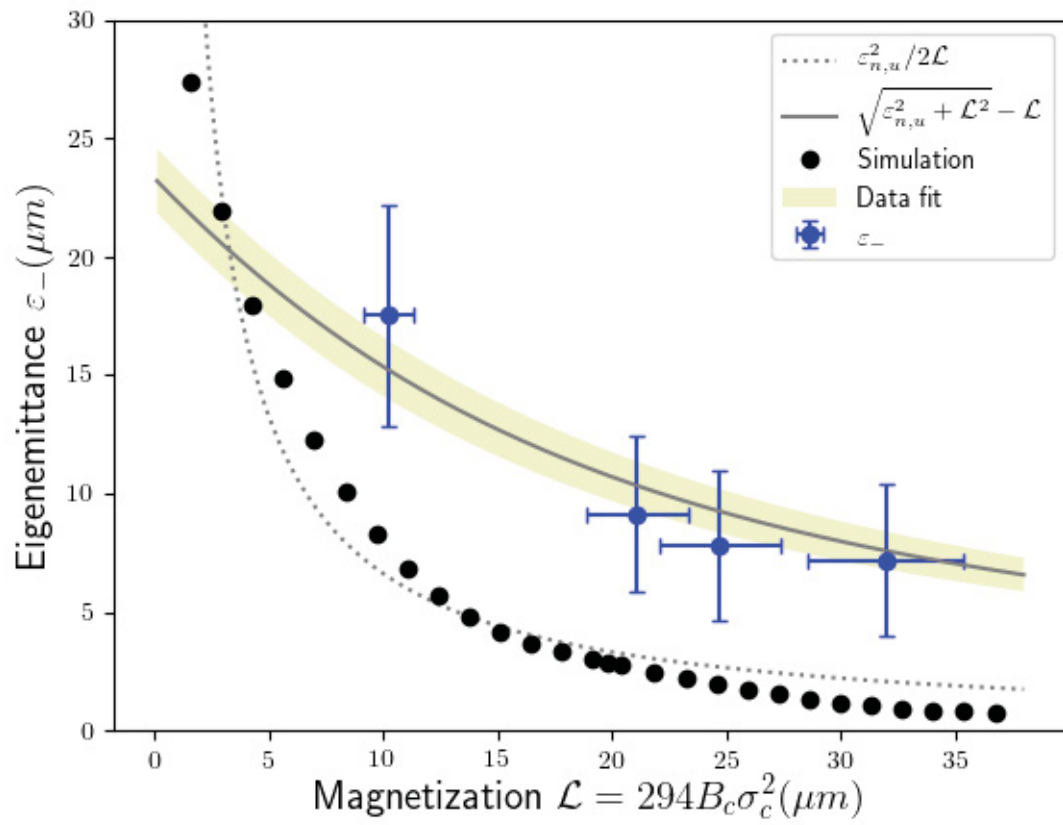


Figure 4.10: Eigen emittance minus experimental data plotted against the calculated magnetization for the 3.2 nC case

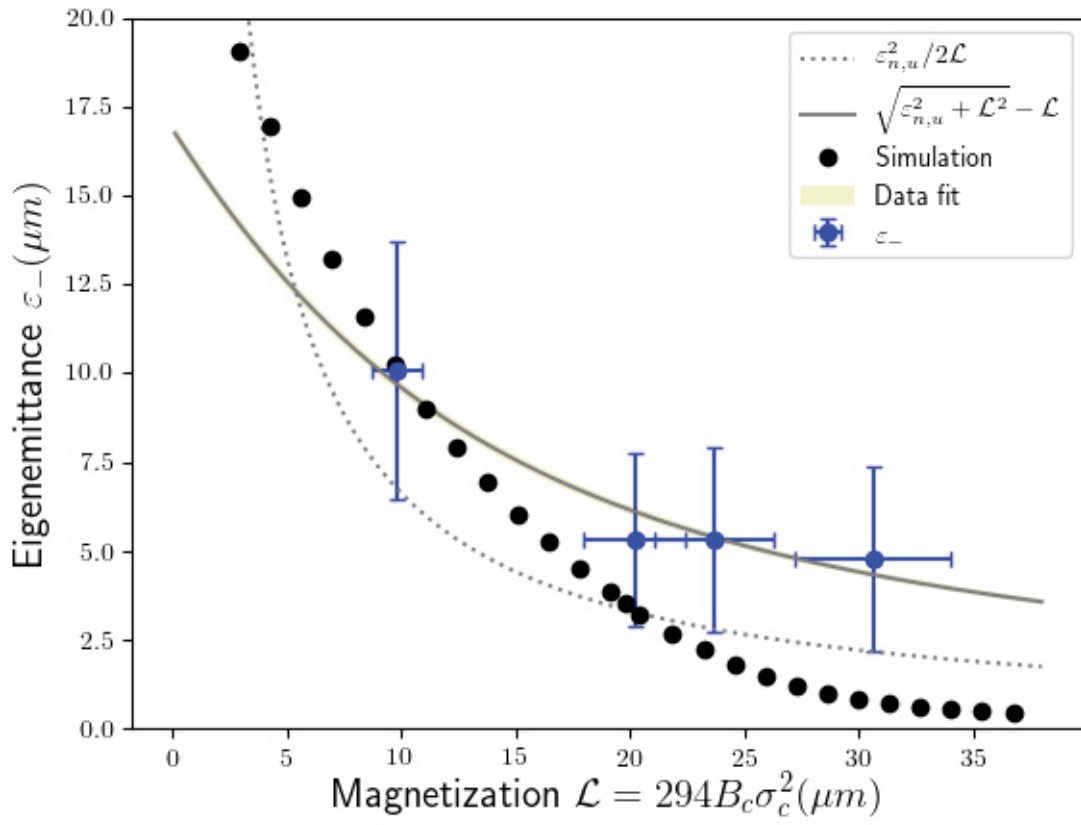


Figure 4.11: Eigen emittance minus experimental data plotted against the calculated magnetization for the 1.6 nC case

CHAPTER 5

CONCLUSION

5.1 Summary

In summary, simulations and experiments performed during this research confirm that a high-charge magnetized bunch with eigen-emittance partition relevant for electron-cooling application in an electron-ion collider could be produced in a photoinjector. These results confirm the assumption made in the electron-cooler design for the JLEIC proposal. We should point out that the beam emittance measured at FAST are obtained with an electron beam with much higher peak current than the one considered for JLEIC. Therefore, the cyclotron emittance is most likely an upper limit and better performances will be likely attained at lower peak current.

In the process of performing extensive simulations, we also uncovered that high-charge magnetized beams seem prone to halo formation and it is currently unclear whether such an effect would ultimately have an impact on the ability to produce the required average beam current for electron cooling.

Finally, we should note that although the research presented in this Thesis was performed in the context of the JLEIC project most of the results could have application to the EIC project to support a possible magnetized-cooling options, e.g., at early stage of the project before more flexible but riskier cooling technique based on coherent electron cooling could be fully deployed.

5.2 Future Work

This work has shown reasonable correlation of expected theoretical, simulation and experimental results of the eigen emittances achievable at the FAST facility. Thus a good promising start in investigating the potential of using electron cooling at 3.2 or 1.6 nC beam charge levels for strong hadron cooling at an EIC. A list of things that should be investigated further are given as suggestions of investigation for future work below.

- Develop an experiment to investigate halo formation in magnetized beams.
- Explore the transport of magnetized beam over long distances using quadrupole-magnet focusing set to provide a globally cylindrical-symmetric beam (to ensure conservation of angular momentum).
- Perform detailed simulations and associated experiment to produce magnetized beam with the lower four-dimensional emittances.

The halo formation observed in the simulation appears to be caused when space charge and magnetization are both present. A combination of the two appear to be causing this instability and may be able to be minimized by optimizing the photo-cathode solenoid settings. This has not been thoroughly investigated in this research and should be a topic of future investigations.

One limitation that was experienced in this research was the non-ideal cylindrical-symmetry of the photocathode-laser distribution on the cathode. This significantly impacts the eigen-emittance partition. Therefore improving the transverse laser distribution should be considered for future experiments. A promising technique implemented at the Argonne Wakefield Accelerator (AWA) consists in producing a homogeneous laser distribution using micro-lens arrays [19].

The experimental preservation of magnetization during beam transport over long distances with quadrupole-magnet focusing could also be investigated at FAST given the accelerator configuration (total length of 100 m).

REFERENCES

- [1] A. Accardi, J. L. Albacete, M. Anselmino, N. Armesto, E. C. Aschenauer, A. Bacchetta, D. Boer, W. K. Brooks, T. Burton, N. B. Chang, W. T. Deng, A. Deshpande, M. Diehl, A. Dumitru, R. Dupré, R. Ent, S. Fazio, H. Gao, V. Guzey, H. Hakobyan, Y. Hao, D. Hasch, R. Holt, T. Horn, M. Huang, A. Hutton, C. Hyde, J. Jalilian-Marian, S. Klein, B. Kopeliovich, Y. Kovchegov, K. Kumar, K. Kumerički, M. A. C. Lamont, T. Lappi, J. H. Lee, Y. Lee, E. M. Levin, F. L. Lin, V. Litvinenko, T. W. Ludlam, C. Marquet, Z. E. Meziani, R. McKeown, A. Metz, R. Milner, V. S. Morozov, A. H. Mueller, B. Müller, D. Müller, P. Nadel-Turonski, H. Paukkunen, A. Prokudin, V. Ptitsyn, X. Qian, J. W. Qiu, M. Ramsey-Musolf, T. Roser, F. Sabatié, R. Sassot, G. Schnell, P. Schweitzer, E. Sichtermann, M. Stratmann, M. Strikman, M. Sullivan, S. Taneja, T. Toll, D. Trbojevic, T. Ullrich, R. Venugopalan, S. Vigdor, W. Vogelsang, C. Weiss, B. W. Xiao, F. Yuan, Y. H. Zhang, and L. Zheng, “Electron ion collider: The next qcd frontier - understanding the glue that binds us all,” 2012.
- [2] D. A. Edwards and M. J. Syphers, *An Introduction to the Physics of High Energy Accelerators*. New York: Wiley, 1993.
- [3] G. Budker, “An effective method of damping particle oscillations in proton and antiproton storage rings,” *Atomnaya Energiya*, pp. 438–440, 1967.
- [4] J. Taylor and S. Taylor, *Classical Mechanics*. University Science Books, 2005.
- [5] Y. S. Derbenev, “Theory of electron cooling,” 2017.

- [6] S. Nagaitsev, L. Prost, and A. Shemyakin, “Fermilab 4.3 mev electron cooler,” *Journal of Instrumentation*, vol. 10, p. T01001, Jan 2015.
- [7] Y. Sun, *Angular-Momentum-Dominated Electron Beams and Flat-Beam Generation*. PhD thesis, Chicago U., 2005.
- [8] A. Burov, S. Nagaitsev, and Y. Derbenev, “Circular modes, beam adapters, and their applications in beam optics,” *Phys. Rev. E*, vol. 66, p. 016503, Jul 2002.
- [9] Y. S. Derbenev, “Prospects of high energy electron cooling,” in *Proceedings of EPAC 2000*, no. 7 in European Particle Accelerator Conference, (Geneva, Switzerland), pp. 8–12, JACoW Publishing, Aug. 2000.
- [10] A. Burov, S. Nagaitsev, A. Shemyakin, and Y. Derbenev, “Optical principles of beam transport for relativistic electron cooling,” *Phys. Rev. ST Accel. Beams*, vol. 3, p. 094002, Sep 2000.
- [11] Y.-E. Sun, P. Piot, K.-J. Kim, N. Barov, S. Lidia, J. Santucci, R. Tikhoplav, and J. Wennerberg, “Generation of angular-momentum-dominated electron beams from a photoinjector,” *Phys. Rev. ST Accel. Beams*, vol. 7, p. 123501, Dec 2004.
- [12] E. Thrane *et al.*, “Photoinjector production of a flat electron beam,” *Proceedings of LINAC, Gyeongju, Korea*, 2002.
- [13] K.-J. Kim, “Round-to-flat transformation of angular-momentum-dominated beams,” *Phys. Rev. ST Accel. Beams*, vol. 6, p. 104002, Oct 2003.
- [14] F. Hannon and M. Stefani, “Transverse uncorrelated emittance diagnostic for magnetized electron beams,” *Phys. Rev. Accel. Beams*, vol. 22, p. 102801, Oct 2019.
- [15] L. Groening, C. Xiao, and M. Chung, “Extension of busch’s theorem to particle beams,” *Phys. Rev. Accel. Beams*, vol. 21, p. 014201, Jan 2018.

- [16] J. Zhu, P. Piot, D. Mihalcea, and C. R. Prokop, “Formation of compressed flat electron beams with high transverse-emittance ratios,” *Phys. Rev. ST Accel. Beams*, vol. 17, p. 084401, Aug 2014.
- [17] J. Qiang, S. Lidia, R. D. Ryne, and C. Limborg-Deprey, “Three-dimensional quasistatic model for high brightness beam dynamics simulation,” *Phys. Rev. ST Accel. Beams*, vol. 9, p. 044204, Apr 2006.
- [18] M. Borland, “Elegant: A flexible sdds-compliant code for accelerator simulation,” *Advanced Photon Source LS-287*, Sept. 2000.
- [19] A. Halavanau, *Electron Beam Shaping and its Applications*. PhD thesis, Northern Illinois University, 2018.
- [20] T. X. et al, “Generation High-Charge of Flat Beams at the Argonne Wakefield Accelerator,” in *Proc. 10th International Particle Accelerator Conference (IPAC’19), Melbourne, Australia, 19-24 May 2019*, no. 10 in International Particle Accelerator Conference, (Geneva, Switzerland), pp. 3337–3340, JACoW Publishing, Jun. 2019. <https://doi.org/10.18429/JACoW-IPAC2019-WEPTS094>.
- [21] P. Piot, “private communication with p. Piot,” Feb. 2019. unpublished work.
- [22] E. D. Courant and H. S. Snyder, “Theory of the alternating gradient synchrotron,” *Annals Phys.*, vol. 3, pp. 1–48, 1958. [Annals Phys.281,360(2000)].